sustainability

MDPI

Article

Preparation of Alkali–Fe-Modified Biochar from Agricultural Waste for Remediation of Cadmium-Contaminated Soil and Water

Xinyue Zhang [1], Dexin Shan [1,*], Yufu Xie [1], Jun Li [1,2], Jingyuan Ning [1], Guangli Yi [1], Huimin Chen [1] and Tingfen Xiang [1]

[1] Chongqing Key Laboratory for Germplasm Innovation of Special Aromatic Spice Plants, Research Institute for Special Plants, College of Smart Agriculture, Chongqing University of Arts and Sciences, Chongqing 402160, China; 15688830307@163.com (X.Z.); 15223986302@163.com (Y.X.); 15196122982@163.com (J.L.); 18725921087@163.com (J.N.); 15002394213@163.com (G.Y.); c19950606893@163.com (H.C.); m15095829421@163.com (T.X.)

[2] Three Gorges Reservoir Area Environment and Ecology of Chongqing Observation and Research Station, Chongqing 404100, China

* Correspondence: 20190006@cqwu.edu.cn; Tel.: +86-13752828417

Abstract

Remediating cadmium (Cd) contamination in aquatic and terrestrial environments has become an urgent environmental priority. Biochar has been widely employed for heavy metal removal due to its wide availability, strong adsorption capacity, and potential for recycling agricultural waste. In this study, samples of alkali–Fe-modified biochar (Fe@NaOH-SBC, Fe@NaOH-HBC, and Fe@NaOH-MBC) were prepared from agricultural wastes (ginger straw, Sichuan pepper branches, and kiwi leaves) through NaOH and $FeCl_3 \cdot 6H_2O$ modification. A comprehensive characterization confirmed that the alkali–Fe-modified biochar exhibits a higher specific surface area, richer functional groups, and successful incorporation of the iron oxides Fe_3O_4 and α-FeOOH. The fitting parameter qmax from the Langmuir model indicates that the alkali–Fe modification of carbon significantly enhanced its maximum capacity for Cd^{2+} adsorption. Furthermore, a synergistic effect was observed between iron oxide loading and alkali modification, outperforming alkali modification alone. Furthermore, a 30-day soil incubation experiment revealed that the application of alkali–Fe-modified biochar significantly increased soil pH, SOM, and CEC while reducing the available cadmium content by 13.34–33.94%. The treatment also facilitated the transformation of highly bioavailable cadmium species into more stable, less bioavailable forms, thereby mitigating their potential entry into the food chain and the associated human health risks. Moreover, short-term spinach seed germination experiments confirmed that treatments with varying additions of alkali–Fe-modified biochar mitigated the inhibition of seed physiological processes by high concentrations of available cadmium to varying degrees. Overall, this study provides a sustainable and effective strategy for utilizing agricultural waste in the remediation of cadmium-contaminated water and soil systems.

Keywords: agricultural waste recycling; modified biochar; heavy metals; adsorption process; soil remediation

Academic Editor: Shibao Chen

Received: 30 October 2025
Revised: 12 December 2025
Accepted: 15 December 2025
Published: 30 December 2025

1. Introduction

In recent years, the rapid expansion of industrial activities has resulted in the discharge of substantial amounts of toxic and hazardous heavy metals into rivers and groundwater,

causing severe environmental contamination [1,2]. Heavy metal pollution in agricultural soils has emerged as a growing global concern, attracting increasing attention [3]. In China, cadmium (Cd) has been identified as the predominant heavy metal contaminant, affecting more than 13,000 hectares of farmland [4,5]. Due to its high toxicity and mobility, Cd(II) readily accumulates in soil–plant systems and enters the food chain, posing a serious threat to human health [6]. Consequently, the development of cost-effective and efficient remediation technologies for Cd(II)-contaminated wastewater and soils has become a critical challenge that urgently needs addressing.

The utilization of agricultural waste to prepare heavy metal adsorbents has been recognized as a promising approach owing to its wide availability, low cost, and environmental friendliness [7]. Biochar—a carbon-rich material produced via the pyrolysis of agricultural biomass under oxygen-limited conditions [8]—has demonstrated strong adsorption potential for heavy metals due to its large specific surface area, well-developed pore structure, and abundant surface functional groups [9]. With its simple preparation process, ecocompatibility, and renewable nature, biochar shows great promise for remediating Cd(II) contamination in both aqueous and soil environments. Moreover, previous studies have reported that biochar represents one of the most rapid and effective strategies for reducing the mobility and bioavailability of toxic metals in soils [10,11].

Beyond conventional biochar systems, recent studies have explored other innovative and recyclable materials for heavy metal removal. For example, Xu et al. (2024) developed a zeolite-loaded cellulose–polyacrylamide hydrogel (Z@CA) for removing cadmium from contaminated soil, which exhibited a high adsorption capacity of 84.4 $mg \cdot g^{-1}$ for Cd(II) and maintained excellent recovery and structural integrity over multiple cycles, demonstrating the potential of hydrogel-based composites in sustainable soil remediation [12].

Nevertheless, several limitations of pristine biochar have been identified with further research. Unmodified biochar generally exhibits a low removal efficiency and limited adsorption capacity toward heavy metal ions, often performing even worse than activated carbon [13]. These shortcomings have restricted its widespread practical application. As a result, researchers have increasingly focused on modifying biochar to enhance its physicochemical properties and adsorption performance for heavy metal remediation.

To overcome these limitations, various modification methods have been developed to improve the adsorption capacity of biochar for heavy metals, including mechanical activation (e.g., ball milling), physical activation (e.g., nitrogen flow treatment), and chemical activation (e.g., KOH or metal oxide loading) [14]. Among these, iron-based modification has received particular attention, as biochar–iron oxide composites have shown excellent potential in removing heavy metals from aqueous and soil environments [15–17]. Iron-modified biochar, produced by incorporating iron compounds or mixtures with biochar, has attracted significant global interest due to its superior adsorption and immobilization performance, which is attributed to its high surface area, strong structural stability, ability to supply Fe ions, and rich functional groups [18,19].

The development of high-performance adsorbents is not limited to heavy metal remediation but also extends to the treatment of radioactive contaminants. In a comprehensive review on radionuclide removal, Ghazoui et al. (2025) [20] highlighted that engineered biochars, such as sewage-sludge-derived and Fe_3O_4-modified biochars, exhibit remarkably high adsorption capacities (e.g., 454.5 $mg \cdot g^{-1}$ for U(VI)), surpassing those of many traditional materials like clays and zeolites. This underscores the ongoing innovation in carbonaceous adsorbents and their potential in addressing diverse environmental pollution challenges.

In addition, alkali modification can further improve the physicochemical properties of biochar by increasing its surface area, functional group density, and alkalinity. For

instance, NaOH-modified rapeseed straw biochar exhibited an increase in specific surface area (SBET) from 19.13 to 43.18 m^2 g^{-1}, resulting in a 1.21-fold improvement in Cd(II) adsorption capacity [21]. Similarly, Ca $(OH)_2$-modified soybean straw biochar achieved a maximum Cd(II) adsorption capacity of 78.49 mg g^{-1}, representing a 1.56-fold enhancement compared with unmodified biochar [22].

Therefore, in this study, a one-step impregnation–pyrolysis method was employed using ginger straw, Sichuan pepper branches and leaves, and kiwifruit branches and leaves as raw materials. Through combined alkali and iron modifications, we developed an alkali–Fe-modified biochar with high efficiency, cost-effectiveness, and environmental sustainability. The prepared biochar was applied for Cd(II) remediation in both aqueous and soil systems, aiming to provide a valuable reference for the restoration of Cd(II)-contaminated environments and to promote the resource utilization of agricultural wastes.

2. Materials and Methods

2.1. Materials and Reagents

The soil used in this study was collected from a kiwifruit plantation located in Yongchuan District, Chongqing, China, which had not been subjected to cadmium contamination. The raw materials—ginger stalks, Sichuan pepper branches, and kiwifruit leaves—were obtained from the experimental base of the Chongqing University of Arts and Sciences. The main chemical reagents included cadmium chloride dihydrate ($CdCl_2 \cdot 2.5H_2O$, analytical grade), sodium hydroxide (NaOH, analytical grade), and nitric acid (HNO_3, analytical grade), which were all purchased from Aladdin Biochemical Technology Co., Ltd., Shanghai, China. Ferric chloride hexahydrate ($FeCl_3 \cdot 6H_2O$, analytical grade) was supplied by Macklin Biochemical Co., Ltd., Shanghai, China. Deionized water was used throughout all experimental procedures for the preparation of analytical-grade solutions. The Cd(II) stock solution was prepared using $CdCl_2 \cdot 2.5H_2O$ as the cadmium source.

2.2. Preparation and Modification of Biochar

2.2.1. Preparation of Raw Biochar

Raw materials, including ginger stalks, Sichuan pepper branches, and kiwifruit leaves, were obtained from the experimental base of Chongqing University of Arts and Sciences. The collected biomass was first rinsed with tap water to remove surface impurities, followed by thorough washing with deionized water. It was then dried at 80 °C for 24 h, cut into approximately 2 cm segments, and ground into 80-mesh powder using a high-speed grinder (model KX-250, Wuyi Dingcang Daily Metal Products Factory, Wuyi, China). The resulting powder was placed in a crucible, covered with aluminum foil, and carbonized in a muffle furnace at 400 °C for 0.5 h. The obtained biochars were designated as SBC (derived from ginger stalks), HBC (from Sichuan pepper branches), and MBC (from kiwifruit leaves) for subsequent experiments.

2.2.2. Preparation of Alkali–Iron-Modified Biochar

SBC, HBC, and MBC were individually immersed in a 1 mol L^{-1} NaOH solution at a solid-to-liquid ratio of 1:10. The mixtures were stirred at 100 °C for 1 h and then allowed to cool naturally. The resulting solids were filtered and rinsed thoroughly with deionized water until a stable pH was achieved, followed by drying at 80 °C. The dried biochar was subsequently soaked in a 1 mol L^{-1} $FeCl_3 \cdot 6H_2O$ solution at a biochar-to-iron mass ratio of 1:1. The pH of the mixture was adjusted to 11 using 5 mol L^{-1} NaOH. After standing for 4 h, the products were washed with deionized water, vacuum-filtered, and dried again at 80 °C before being stored in sealed containers. The final alkali–Fe-modified biochar

specimens were designated as Fe@NaOH-SBC, Fe@NaOH-HBC, and Fe@NaOH-MBC for subsequent experiments.

2.3. Characterization and Analysis

The elemental compositions (C, H, N, and O) of the SBC, HBC, MBC, Fe@NaOH-SBC, Fe@NaOH-HBC, and Fe@NaOH-MBC were determined using an elemental analyzer (Vario EL Cube, Elementar, Langenselbold, Germany). The microstructures and surface morphologies of the six biochar samples were examined using scanning electron microscopy (SEM; Gemini SEM 300, ZEISS, Oberkochen, Germany). The specific surface area, pore volume, and pore size distribution were analyzed using an automated surface area and porosity analyzer (ASAP 2460, Micromeritics, Norcross, GA, USA). The surface functional groups were identified using Fourier-transform infrared spectroscopy (FTIR—Thermo Fisher Scientific Nicolet iS20, Waltham, MA, USA). In addition, X-ray photoelectron spectroscopy (XPS; K-Alpha, Thermo Fisher Scientific, Waltham, MA, USA) was employed to determine the surface elemental composition and chemical bonding states, with high-resolution scans conducted for the C 1s, O 1s, and N 1s regions. The crystalline structures of the biochars were characterized using X-ray diffraction (XRD; Ultima IV, Rigaku, Japan). XPS data were processed using Avantage software, while XRD data were processed using Jade 9 software. Data calculation and processing were completed using Excel. Additionally, Origin 2021 software was employed for adsorption model fitting, and corresponding adsorption model plots and FTIR spectra were generated.

2.4. Adsorption Experiment

Cadmium-containing wastewater was treated via adsorption using six types of biochar material: SBC, NaOH-SBC, Fe@NaOH-SBC, MBC, NaOH-MBC, Fe@NaOH-MBC, HBC, NaOH-HBC, and Fe@NaOH-HBC. To prevent cadmium precipitation during the adsorption process, the initial pH of the Cd(II) solution was adjusted to approximately 5.5 using 0.1 mol L^{-1} HNO_3 or NaOH solutions [23]. After adsorption, the suspensions were filtered, and the residual Cd(II) concentration in the filtrate was determined via flame atomic absorption spectroscopy (FAAS) using a Shimadzu AA-6300C spectrometer (Tokyo, Japan).

2.4.1. Adsorption Kinetics

A 50 mL solution containing Cd(II) was placed in a 100 mL polyethylene centrifuge tube, together with 0.05 g of adsorbent. To ensure the adsorption isotherm experiments with the alkali–Fe-modified carbon (Fe@NaOH-SBC, Fe@NaOH-MBC, Fe@NaOH-HBC), alkali-modified carbon (NaOH-SBC, NaOH-MBC, NaOH-HBC), and raw carbon (SBC, MBC, HBC) could be conducted within their pre-experimentally determined effective adsorption capacity ranges to obtain high-quality, fit-ready data, we purposefully set different initial concentrations: 50 mg L^{-1} for raw carbon, 100 mg L^{-1} for alkali-modified carbon, and 150 mg L^{-1} for alkali–Fe-modified carbon. The pH was adjusted to 5.00 ± 0.05, and the mixture was shaken at 150 rpm and 25 °C for 24 h. Aliquots were withdrawn at predetermined time intervals (0, 1, 5, 10, 30, 60, 120, 240, 480, and 1440 min) and filtered through a 0.45 μm disposable organic syringe filter, and the filtrate was analyzed for Cd(II) concentration using flame atomic absorption spectroscopy (FAAS) with a Shimadzu AA-6300C spectrometer (Tokyo, Japan) at a 277.7 nm wavelength.

2.4.2. Adsorption Isotherms

A series of 50 mL Cd(II) solutions with initial concentrations ranging from 0.5 to 400 mg L^{-1} was prepared in 100 mL conical flasks. The initial pH of each solution was adjusted to 5.50 ± 0.05. Subsequently, 0.05 g of adsorbent was added to each flask, and the

mixtures were shaken at 150 rpm and 25 °C for 24 h. After shaking, the suspensions were filtered, and the filtrates were analyzed to identify any residual Cd(II) concentration.

2.4.3. Adsorption Thermodynamics

In 100 mL polyethylene centrifuge tubes, 0.05 g of adsorbent and 50 mL of a 200 mg L^{-1} Cd(II) solution were added. The pH was adjusted to 5.00 ± 0.05. The tubes were then incubated in a constant-temperature shaker at 150 rpm for 24 h at three different temperatures (25, 35, and 45 °C). After incubation, the mixtures were filtered, and the filtrates were analyzed to identify any residual Cd(II) concentration. All adsorption experiments were performed in triplicate, and the results are reported as mean values.

2.5. Soil Incubation Experiment for Heavy Metal Remediation

In this study, surface soil samples (0–20 cm depth) were collected from a kiwifruit plantation in Yongchuan District, Chongqing Municipality, which was an area without prior cadmium contamination. The soil here is typical purple soil. The samples were air-dried, mechanically ground, and passed through a 2 mm sieve. To meet the experimental requirements, cadmium was introduced by adding a cadmium chloride ($CdCl_2$) solution to the soil. The solution was applied evenly and thoroughly mixed to ensure a homogeneous distribution. The soil moisture content was then adjusted to 80% of the field capacity using deionized water. Subsequently, the spiked soils were incubated for one month at room temperature in sealed containers under dark conditions to prevent photodegradation and minimize moisture loss. The deionized water was replenished every three days during incubation to maintain the soil moisture at 80% [24]. After one month of soil passivation, a spinach seed germination experiment was conducted.

2.6. Determination of Soil-Related Indexes

The collected soil samples were air-dried, homogenized, and sequentially passed through 20- and 100-mesh sieves (HJ/T 166-2004) [25]. The fraction retained on the 100-mesh sieve was subjected to a five-step sequential extraction procedure following the Tessier method to determine the cadmium speciation [26]. In contrast, the fraction that passed through the 20-mesh sieve was used to analyze the pH, CEC, and SOM, and available cadmium contents.

3. Results and Discussion

3.1. Characterization of the Biochar

3.1.1. Basic Characteristics of Biochar

The atomic ratios of different elements can determine the chemical properties of biochar to some extent. The elemental compositions of HBC, MBC, and SBC are shown in Table 1.

Table 1. Basic characteristics of HBC, MBC, and SBC.

Biochar	N (%)	C (%)	H (%)	O (%)	H/C	O/C	(O + N)/C	Ash Content (%)
SBC	2.304	52.493	3.814	20.939	0.865	0.299	0.337	26
HBC	1.517	62.802	4.022	22.510	0.763	0.269	0.290	10
MBC	1.120	68.264	4.086	21.921	0.713	0.241	0.255	7

When characterizing the fundamental chemical properties of biochar, the atomic ratios H/C, O/C, and (N + O)/C are commonly calculated based on the percentage compositions of C, H, O, and N elements. Table 1 shows that the H/C atomic ratios of SBC, HBC,

and MBC are all <1, with MBC exhibiting the lowest H/C ratio (0.713), indicating its highly carbonized state [27]. High carbonization facilitates the formation of more aromatic structures. When the H/C ratio is low, biochar exhibits strong aromaticity and high stability. The O/C ratio reflects the hydrophilicity of the biochar surface; higher values indicate stronger hydrophilicity [28]. The (N + O)/C ratio represents the abundance of polar functional groups; higher values indicate greater biochar polarity. SBC exhibits the highest atomic ratios (O/C = 0.299, (O + N)/C = 0.337), indicating strong hydrophilicity, which is conducive to chelating heavy metal ions (e.g., Pb^{2+}, Cd^{2+}). This suggests the presence of abundant oxygen/nitrogen-containing functional groups (e.g., -COOH, -OH), which were verified via a subsequent FTIR analysis of the biochar.

3.1.2. Microstructure of Biochar

1. Surface morphology analysis

The surface morphologies of SBC (a), Fe@NaOH-SBC (b), HBC (c), Fe@NaOH-HBC (d), MBC (e), and Fe@NaOH-MBC (f) were observed using SEM.

Figure 1a,c,e show that SBC, HBC, and MBC exhibited typical porous structures characterized by relatively intact pore networks and well-organized arrangements. The original tubular morphology was largely retained with smooth surface features. In contrast, observations of the Fe-modified biochars (Fe@NaOH-SBC, Fe@NaOH-HBC, and Fe@NaOH-MBC) at the same magnification (Figure 1b,d,f) revealed partial structural collapse and fragmentation of the initially regular surfaces, likely caused by corrosion during the NaOH treatment in the modification process. The modified biochar displayed irregular surface textures covered with numerous fine particles, which were presumably iron oxides formed during the alkali-iron modification. These deposited particles contributed to a rougher surface morphology and the formation of additional irregular structures, which increased the number of active adsorption sites and substantially enlarged the specific surface area. Such structural alterations were expected to enhance the metal ion adsorption capacity of the Fe-modified biochar [29].

2. Specific surface area and pore structure analysis

Table 2 shows the specific surface area, total pore volume, and average pore size of the HBC, MBC, SBC, Fe@NaOH-SBC, Fe@NaOH-HBC, and Fe@NaOH-MBC (calculated using the BET method).

Table 2. Analysis of specific surface area and pore structure of biochars SBC, Fe@NaOH-SBC, HBC, Fe@NaOH-HBC, MBC, and Fe@NaOH-MBC.

Biochar	BET Specific Area (m^2/g)	Total Pore Volume (Adsorption) (cm^3/g) 10^{-2}	BET Average Pore Size (Adsorption) (nm)
SBC	3.707	1.03	11.152
Fe@NaOH-SBC	67.096	5.22	3.115
HBC	2.703	0.56	8.274
Fe@NaOH-HBC	45.229	8.17	7.217
MBC	3.559	0.83	9.319
Fe@NaOH-MBC	67.369	5.57	3.307

The alkali–Fe-modified biochars (Fe@NaOH-SBC, Fe@NaOH-HBC, and Fe@NaOH-MBC) exhibited markedly increased specific surface areas, confirming the effectiveness of the modification process in improving the surface characteristics, a result consistent with previous findings [30]. The total pore volumes of Fe@NaOH-SBC, Fe@NaOH-HBC, and Fe@NaOH-MBC increased by factors of 5.2, 14.5, and 6.7, respectively. Since a larger

pore volume generally correlates with an enhanced adsorption capacity, these results indicate that the modified biochars possess significantly improved adsorption performance compared with their unmodified counterparts. Notably, Fe-SBC and Fe-HBC displayed the most pronounced reductions in average pore size. The modification process further refined the pore structure, transitioning from larger to smaller mesopores within the mesoporous range. Mesopores provide an optimal balance between diffusion efficiency and adsorption capacity while offering a higher specific surface area than macropores, as supported by the surface area data [31]. In summary, NaOH, serving as an alkaline modifier, selectively dissolved silicate and ash components within the biochar matrix, thereby generating new micropores and mesopores [32]. Concurrently, $FeCl_3 \cdot 6H_2O$ acted as the iron source, producing iron oxide deposits that subdivided macropores into mesoporous structures with enlarged surface areas. Together, these modifications contributed to the increased specific surface area, total pore volume, and reduced average pore size of the treated biochar. Such textural enhancements are expected to substantially improve the heavy metal adsorption capacity of the alkali–Fe-modified biochar.

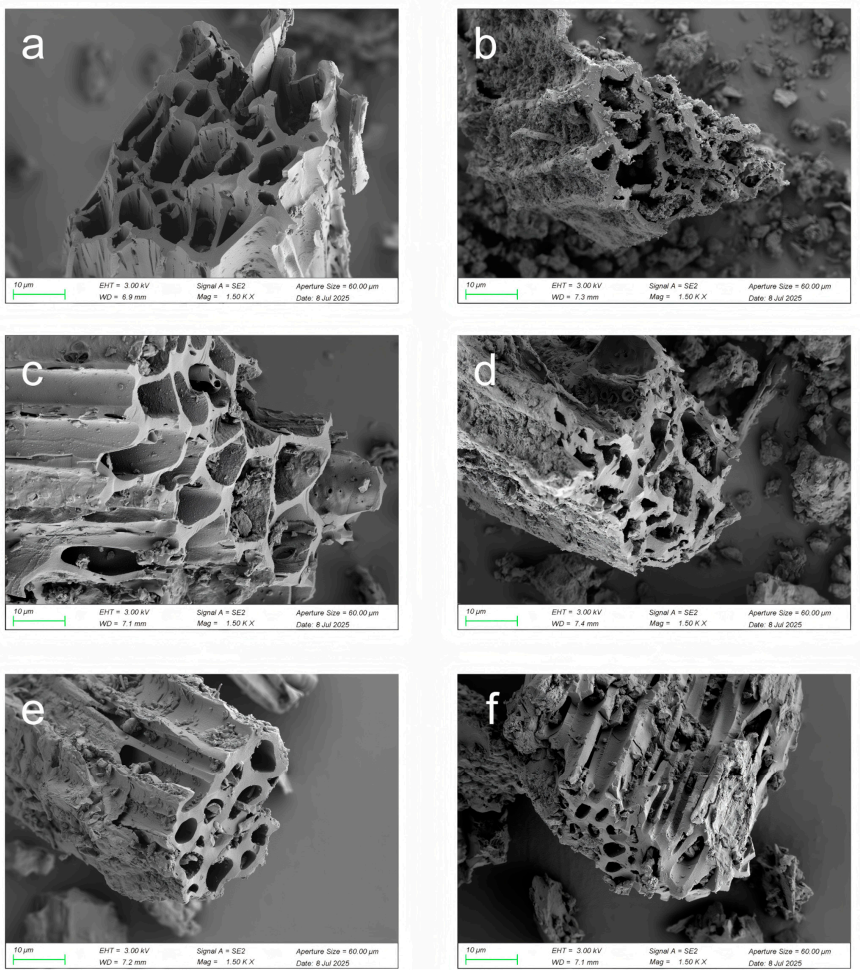

Figure 1. SEM diagrams of carbon materials: (**a**) SBC, (**b**) Fe@NaOH-SBC, (**c**) HBC, (**d**) Fe@NaOH-HBC, (**e**) MBC, and (**f**) Fe@NaOH-MBC.

3.1.3. FTIR Analysis

FTIR was employed to analyze the surface functional groups of the SBC, Fe@NaOH-SBC, HBC, Fe@NaOH-HBC, MBC, and Fe@NaOH-MBC, and the results are presented in Figure 2.

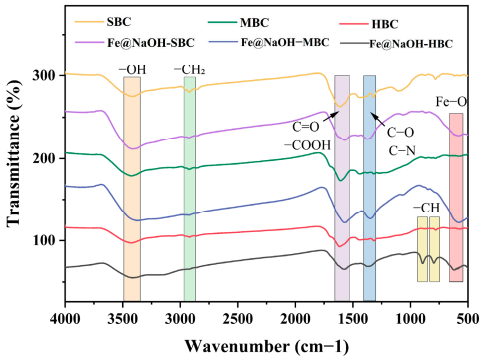

Figure 2. The FTIR spectra of SBC, Fe@NaOH-SBC, HBC, Fe@NaOH-HBC, MBC, and Fe@NaOH-MBC.

Fourier transform infrared (FTIR) analysis of the biochar samples revealed significant changes in functional groups before and after modification. The broad absorption peak observed at 3415–3419 cm^{-1} corresponds to O-H stretching vibrations [33]. Following the alkali–Fe modification, the intensity of this peak markedly increased and shifted toward lower frequencies (3415–3390 cm^{-1}), indicating the introduction of additional hydroxyl groups [34]. This modification enhanced hydrogen-bonding interactions and the ion-exchange capacity of the biochar surface [35]. The absorption peak near 2925 cm^{-1} in the original biochar (SBC, MBC, HBC) corresponds to the asymmetric stretching vibration of $-CH_2$ in the fatty chain, indicating the presence of aliphatic structures [36]. After the alkali–Fe modification, this peak nearly disappears, suggesting that the aliphatic components were consumed or transformed during the strong alkali modification process. Absorption peaks at 1602–1612 cm^{-1} are typically attributed to aromatic C=C stretching vibrations or C=O stretching vibrations in carboxyl groups (-COOH) [37]. Following the alkali–Fe modification, this peak shifts to 1566–1568 cm^{-1}. The red shift at both positions may result from the introduction of oxygen-containing functional groups during alkali modification, which facilitates ion-exchange adsorption and plays a crucial role in stabilizing heavy metals in soil [38]. The absorption peak at 1314–1317 cm^{-1} likely originates from C-O or C-N stretching vibrations [39], exhibiting a blue shift to 1344–1370 cm^{-1} after modification. This blue shift, combined with the aforementioned functional group changes, provides key evidence for functional group rearrangement, which facilitates the formation of surface complexes with metal ions [40].

Notably, new absorption peaks at 613–580 cm^{-1} appeared in Fe@NaOH-SBC, Fe@NaOH-MBC, and Fe@NaOH-HBC, which were unequivocally attributed to Fe-O bond-stretching vibrations. This confirms the successful loading of iron oxides onto the biochar surface [41]. The introduction of iron oxides not only provides specific adsorption sites but may also enhance heavy metal immobilization through coprecipitation. Fe-HBC exhibits two new absorption peaks between 895 and 796 cm^{-1}. According to literature reports, this wavenumber range is characteristic of the out-of-plane bending vibration of C-H bonds on aromatic rings [42–44]. This vibrational mode serves as a crucial basis for determining the substitution type of aromatic structures, and its appearance directly confirms the presence of aromatic structures in the modified biochar. The existence of aromatic systems provides the structural basis for π–π interactions [45], a mechanism that plays a significant role in the adsorption of heavy metals, such as Cd^{2+}.

3.1.4. XPS Analysis

X-ray photoelectron spectroscopy (XPS) was employed to analyze changes in the surface properties of biochar before and after modification. The full-scan XPS spectra and high-resolution narrow scans of C 1s, O 1s, and N 1s for the modified biochar are presented in Figures 3 and 4.

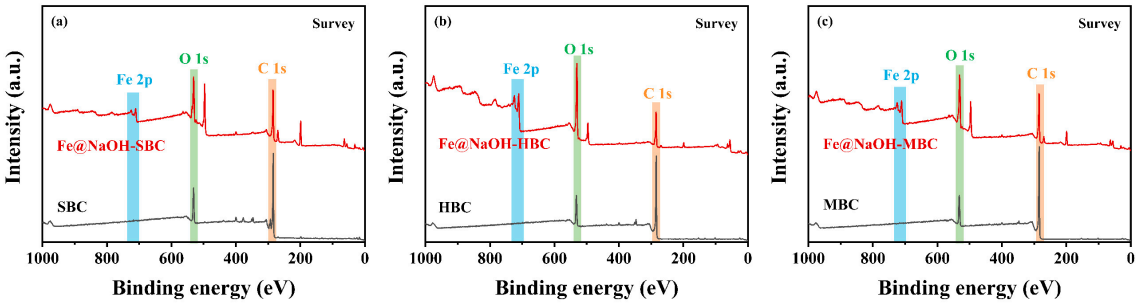

Figure 3. The XPS spectra of (**a**) SBC and Fe@NaOH-SBC, (**b**) HBC and Fe@NaOH-HBC, and (**c**) MBC and Fe@NaOH-MBC.

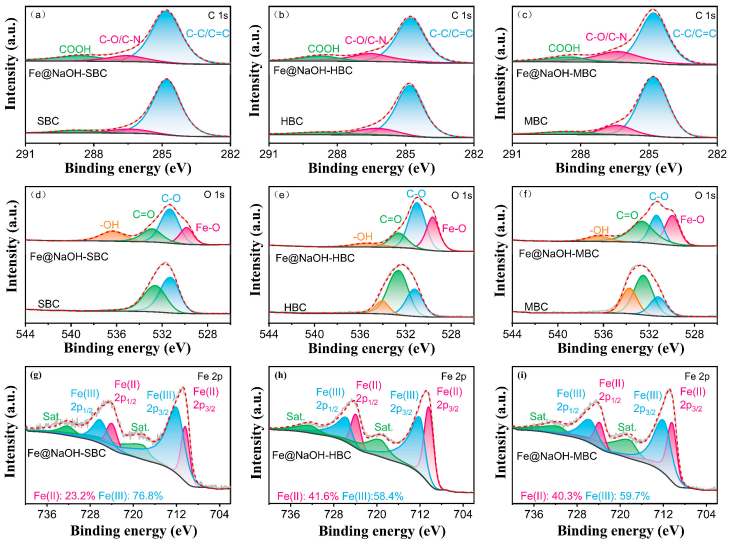

Figure 4. (**a**–**i**) The high-resolution C 1s, O 1s, and Fe 2p spectra of SBC, Fe@NaOH-SBC, HBC, Fe@NaOH-HBC, MBC, and Fe@NaOH-MBC.

The XPS full-scan spectra of the biochar before and after modification—SBC and Fe@NaOH-SBC, HBC and Fe@NaOH-HBC, and MBC and Fe@NaOH-MBC—are presented in Figure 3a–c. All spectra displayed characteristic peaks corresponding to C 1s at approximately 284 eV, O 1s near 531 eV, and N 1s around 398 eV. In the modified samples (Fe@NaOH-SBC, Fe@NaOH-HBC, and Fe@NaOH-MBC), additional Fe 2p peaks appeared in the range of 700–740 eV, confirming the successful incorporation of iron species onto the biochar surfaces.

In Figure 4, the C1s spectra of SBC, XBC, and HBC (Figure 4a–c) can be resolved into three peaks with binding energies (BEs) near 284.8, 286.6, and 288.7 eV, corresponding to the functional groups C-C/C=C, C-O/C-N, and -COOH, respectively. Following alkaline-iron modification, the C1s spectra of Fe@NaOH-SBC, Fe@NaOH-MBC, and Fe@NaOH-HBC exhibit significant changes in the relative intensities of these three peaks, with substantial increases in the C-O/C-N and -COOH contents. This phenomenon primarily stems from oxidation reactions induced by the alkaline modifier. Under alkaline conditions, the carbon skeleton undergoes etching and degradation, oxidizing some stable C-C/C=C structures and introducing oxygen-containing functional groups, such as carboxyl (-COOH), hydroxyl (-OH), and ether bonds (C-O). This is crucial for enhancing the adsorption performance of heavy metal Cd^{2+}. Concurrently, the content of C-C/C=C components, representing the original biochar skeleton, correspondingly decreased. This directly confirms that the modification process disrupted part of the aromatic structure and successfully converted it into various oxygen-containing functional groups. These functional groups serve as

excellent metal-ion coordination sites, effectively immobilizing Cd^{2+} through ion exchange and surface complexation mechanisms [46].

The O 1s spectrum (Figure 4d–f) exhibits characteristic peaks for C=O, C-O, and -OH groups. Post-modification, the C=O and -OH contents increased while the C-O content decreased. A new characteristic peak emerged near 530 eV, which was attributable to Fe-O bonds in iron oxides (e.g., Fe_3O_4 or γ-Fe_2O_3) [47,48]. This peak serves as direct evidence that iron oxides were successfully chemically bonded onto the biochar. The concurrent increases in C=O and -OH functional groups indicate that the carbon skeleton of biochar was etched and oxidized under the strongly oxidizing conditions of alkaline iron modification, introducing more oxygen-containing functional groups. Simultaneously, the C=O and –OH functional groups significantly increased while C-O decreased. These changes suggest that the intense oxidation during alkaline iron modification introduced abundant oxygen-containing functional groups onto the biochar surface. The substantial increase in oxygen-containing functional groups (carboxyl, hydroxyl) and iron oxide active sites on the modified carbon surface is expected to synergistically enhance the Cd^{2+} adsorption performance through complexation interactions [49].

Figure 4g–i present the Fe 2p spectra. The photoelectron peaks of the three alkali–Fe-modified carbons in the 710–726 eV range correspond to the binding energies of Fe 2p 3/2 and Fe 2p 1/2. Peaks near 710.4 and 723.9 eV represent Fe^{2+} binding energy peaks [50]; those near 712 and 726 eV indicate Fe^{3+} binding energy peaks [51], with the peak near 726 eV corresponding to α-FeOOH [52]. The binding energy gap between the two main peaks (723.9 and 710.4 eV) is 13.5 eV, indicating the presence of Fe_3O_4 in the material [53]. These results collectively confirm the successful loading of iron oxides onto the three alkali–Fe-modified carbons after the alkali–Fe modification. The Fe(II)/Fe(III) ratios were 41.6%:58.4% for Fe@NaOH-HBC, 40.3%:59.7% for Fe@NaOH-MBC, and 23.2%:76.8% for Fe@NaOH-SBC. By comparing the Fe(II)/Fe(III) ratios across the three alkali–Fe-modified carbon materials, we observed that different biochar feedstocks significantly influence the oxidation states distribution.

3.1.5. XRD Analysis

To further determine the chemical compositions of the six types of biochar in this study, Figure 5a–c show the XRD patterns of SBC and Fe@NaOH-SBC, HBC and Fe@NaOH-HBC, and MBC and Fe@NaOH-MBC.

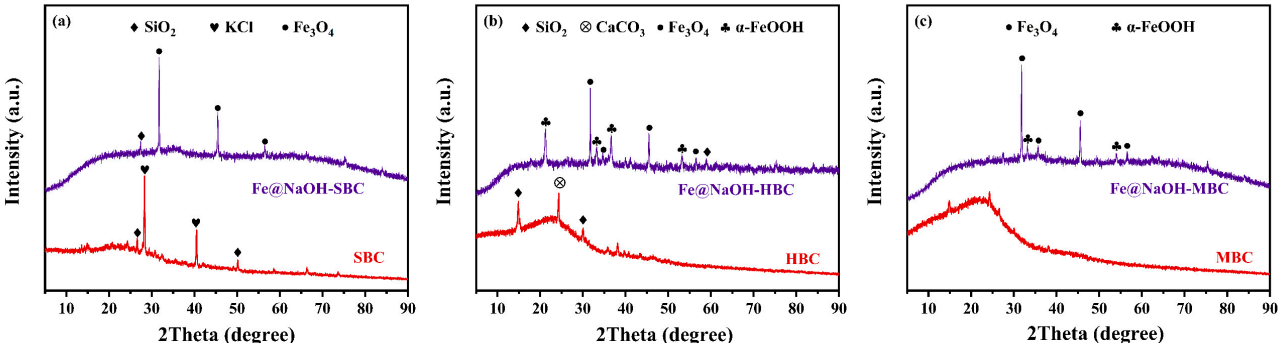

Figure 5. The XRD spectra of (**a**) SBC and Fe@NaOH-SBC, (**b**) HBC and Fe@NaOH-HBC, and (**c**) MBC and Fe@NaOH-MBC.

The XRD patterns of SBC, HBC, and MBC all exhibited a broad diffraction peak near 25°, which can be attributed to the microcrystalline structures and disordered graphitic layers formed during the biomass pyrolysis, confirming the presence of amorphous carbon [54–56]. Additional peaks observed at 26.55°, 50.29°, 14.80°, 30.16°, and 20.95° in SBC,

HBC, and Fe@NaOH-HBC were identified as characteristic of silicon oxide (SiO), likely originating from endogenous mineral components in the ginger stalks and Sichuan pepper branches that remained in the biochar as ash [57]. Moreover, peaks detected in SBC at 28.33° and 40.54° were assigned to KCl, while those appearing in HBC, Fe@NaOH-HBC, and Fe@NaOH-MBC at 24.05° and 36.00° corresponded to the (012) and (110) crystal planes of $CaCO_3$, based on a comparison with the XRD standard card (PDF#05-0586). These crystalline phases are attributed to ash-derived minerals naturally present in the raw biomass.

Unlike raw biochar, the XRD patterns of the alkali–Fe-modified biochars (Fe@NaOH-SBC, Fe@NaOH-HBC, and Fe@NaOH-MBC) show weakened or even absent diffraction peaks of amorphous carbon, which are replaced by multiple sharp peaks corresponding to Fe_3O_4, α-FeOOH, and α-Fe_2O_3. Fe@NaOH-SBC exhibits characteristic Fe_3O_4 peaks at 31.57°, 45.4°, and 56.45° (JCPDS card: No. 19-0629) [58]; Fe@NaOH-MBC exhibits characteristic Fe_3O_4 peaks at 31.88°, 35.65°, 45.56°, and 56.47°, along with α-FeOOH peaks at 33.21° and 53.95° (JCPDS Card: No. 29-0713) [59]; Fe@NaOH-HBC exhibits characteristic peaks for Fe_3O_4 at 32.9°, 34.5°, 45.3°, and 56.37°, and for α-FeOOH at 21.2°, 33.0°, 36.6°, and 53.35°. Alkali–Fe modification successfully loaded crystalline iron oxides (Fe_3O_4, α-FeOOH) onto three types of biochar. However, the use of different biochar feedstocks resulted in distinct final iron phase compositions: Fe@NaOH-SBC primarily loaded Fe_3O_4, while Fe@NaOH-HBC and Fe@NaOH-MBC formed composite phases of Fe_3O_4 and α-FeOOH.

3.2. Adsorption of Cd(II) from Aqueous Solution

3.2.1. Adsorption Kinetics

The pseudo-first-order Equation (S1) and pseudo-second-order Equation (S2) kinetic models were applied to fit the experimental adsorption data. The temporal adsorption behavior of Cd(II) on SBC, NaOH-SBC, Fe@NaOH-SBC, HBC, NaOH-HBC, Fe@NaOH-HBC, MBC, NaOH-MBC, and Fe@NaOH-MBC is illustrated in Figure 6a–i, while the corresponding fitting parameters for each kinetic model are summarized in Tables 3–5.

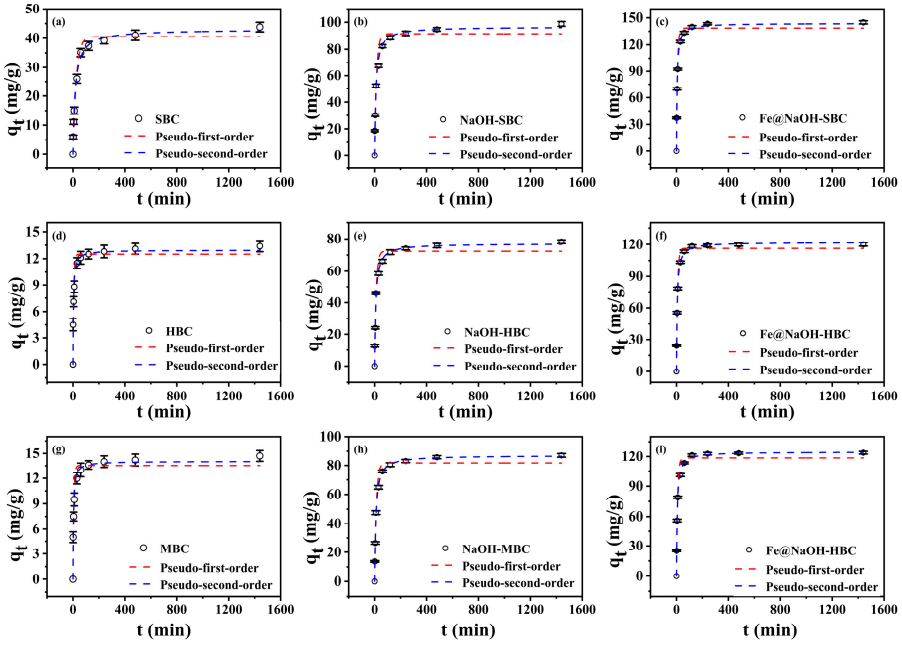

Figure 6. The pseudo-first-order and pseudo-second-order models of (**a**) SBC, (**b**) NaOH-SBC, (**c**) Fe@NaOH-SBC, (**d**) HBC, (**e**) NaOH-HBC, (**f**) Fe@NaOH-HBC, (**g**) MBC, (**h**) NaOH-MBC, and (**i**) Fe@NaOH-MBC for Cd(II) adsorption (contact time: 0–24 h; temperature: 25 °C; initial concentration: 50, 100, or 150 mg/L).

Table 3. Fitting pseudo-second-order (PSO) and pseudo-first-order (PFO) kinetic models for SBC, NaOH-SBC, and Fe@NaOH-SBC for Cd(II) adsorption.

Model	Parameter	SBC	NaOH-SBC	Fe@NaOH-SBC
Pseudo-first-order	qe,exp (mg/g)	43.8	98.8	145.0
	qe,cal (mg/g)	40.515	91.507	138.576
	K_1 (1/min)	0.040	0.070	0.128
	R^2	0.9709	0.9521	0.9642
Pseudo-second-order	qe,cal (mg/g)	43.004	96.661	143.880
	K_2 (g/mg·min)	0.001	0.001	0.002
	R^2	0.9901	0.9863	0.9914

Table 4. Fitting pseudo-second-order (PSO) and pseudo-first-order (PFO) kinetic models for HBC, NaOH-HBC, and Fe@NaOH-HBC for Cd(II) adsorption.

Model	Parameter	HBC	NaOH-HBC	Fe@NaOH-HBC
Pseudo-first-order	qe,exp (mg/g)	13.4	78.3	120
	qe,cal (mg/g)	12.504	72.364	116.243
	K_1 (1/min)	0.161	0.853	0.121
	R^2	0.9333	0.9674	0.9827
Pseudo-second-order	qe,cal (mg/g)	12.946	77.089	121.821
	K_2 (g/mg·min)	0.022	0.002	0.002
	R^2	0.9760	0.9903	0.9973

Table 5. Fitting pseudo-second-order (PSO) and pseudo-first-order (PFO) kinetic models for MBC, NaOH-MBC, and Fe@NaOH-MBC for Cd(II) adsorption.

Model	Parameter	MBC	NaOH-MBC	Fe@NaOH-MBC
Pseudo-first-order	qe,exp (mg/g)	14.7	87.1	124.0
	qe,cal (mg/g)	13.532	81.747	118.603
	K_1 (1/min)	0.157	0.076	0.116
	R^2	0.9203	0.9737	0.9718
Pseudo-second-order	qe,cal (mg/g)	14.047	87.040	124.787
	K_2 (g/mg·min)	0.019	0.001	0.001
	R^2	0.9691	0.9937	0.9959

Figure 6a–i show the removal efficiency of Cd(II) by the nine types of biochar over a 24 h period. The adsorption process exhibited a rapid initial phase, followed by a gradual approach to equilibrium. This behavior can be attributed to the high availability of surface adsorption sites and the elevated Cd(II) concentration at the beginning of the reaction, which facilitated a rapid adsorption rate. As the active sites became progressively occupied and the Cd(II) concentration decreased, the diffusion of Cd(II) ions into the interior pores of the biochar became the rate-limiting step, resulting in a pronounced reduction in the overall adsorption rate.

Based on the parameter fitting results in Tables 3–5, both pseudo-first-order and pseudo-second-order kinetic models can adequately fit the Cd(II) removal of alkali–Fe-modified carbons (Fe@NaOH-SBC, Fe@NaOH-MBC, Fe@NaOH-HBC), NaOH-modified carbons (NaOH-SBC, NaOH-MBC, NaOH-HBC), and native carbons (SBC, MBC, HBC) for Cd(II). The R^2 values for both kinetic models exceed 0.9. Comparison reveals that the correlation coefficient (R^2) for the pseudo-second-order model consistently surpasses

that of the pseudo-first-order model. Furthermore, the calculated adsorption capacity (qe,cal) from the pseudo-second-order model more closely approximates the experimental adsorption value (qe,exp). Therefore, we conclude that the pseudo-second-order kinetic model provides a more accurate fit for the Cd(II) adsorption process.

Furthermore, comparing Tables 3–5 (qe,exp represents the equilibrium adsorption capacity obtained during experiments) reveals that the equilibrium adsorption capacity has the following order: alkali–Fe-modified carbon > NaOH-modified carbon > original carbon. This demonstrates that alkali–Fe composite modification exhibits significant advantages in adsorption capacity. The synergistic effect between iron oxide loading and alkali modification not only shifts the adsorption process toward chemical dominance but also fundamentally enhances the adsorption performance of biochar materials.

3.2.2. Adsorption Isotherms

To further elucidate the adsorption equilibrium characteristics, performance, and underlying mechanisms of Cd(II) adsorption on SBC, NaOH-SBC, Fe@NaOH-SBC, HBC, NaOH-HBC, Fe@NaOH-HBC, MBC, NaOH-MBC, and Fe@NaOH-MBC, the experimental data were fitted using the Langmuir (Equation (S3)) and the Freundlich (Equation (S4)) adsorption isotherm equations. The corresponding fitted curves for the two models are presented in Figure 7a–i, and the model parameters, along with their correlation coefficients (R^2), are summarized in Tables 6–8.

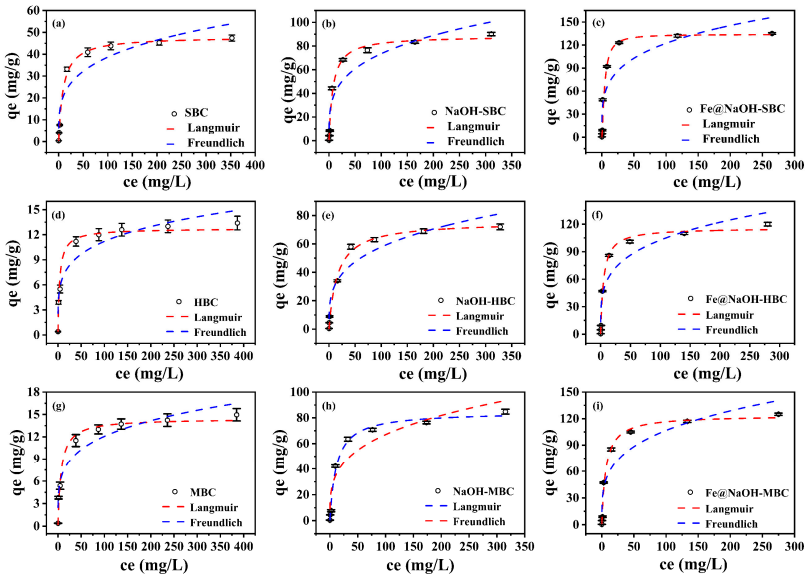

Figure 7. The Freundlich and Langmuir models of (**a**) SBC, (**b**) NaOH-SBC, (**c**) Fe@NaOH-SBC, (**d**) HBC, (**e**) NaOH-HBC, (**f**) Fe@NaOH-HBC, (**g**) MBC, (**h**) NaOH-MBC, and (**i**) Fe@NaOH-MBC for Cd(II) adsorption (contact time: 0–24 h, temperature: 25 °C, initial concentrations: 0.5–400 mg/L).

Table 6. Kinetic characteristics of the Freundlich and Langmuir models for SBC, NaOH-SBC, and Fe@NaOH-SBC during Cd(II) adsorption.

Model	Parameter	SBC	NaOH-SBC	Fe@NaOH-SBC
Langmuir	q_{max} (mg/g)	48.05	88.46	133.91
	K_L (L/mg)	0.107	0.131	0.116
	R^2	0.996	0.988	0.986
Freundlich	K_F (L/mg)	11.449	20.774	38.630
	1/n	0.264	0.274	0.250
	R^2	0.884	0.887	0.817

Table 7. Kinetic characteristics of the Freundlich and Langmuir models for HBC, NaOH-HBC, and Fe@NaOH-HBC during Cd(II) adsorption.

Model	Parameter	HBC	NaOH-HBC	Fe@NaOH-HBC
Langmuir	q_{max} (mg/g)	12.77	75.67	115.97
	K_L (L/mg)	0.306	0.061	0.208
	R^2	0.986	0.993	0.996
Freundlich	K_F (L/mg)	4.223	15.450	32.405
	1/n	0.212	0.287	0.250
	R^2	0.924	0.928	0.903

Table 8. Kinetic characteristics of the Freundlich and Langmuir models for MBC, NaOH-MBC, and Fe@NaOH-MBC during Cd(II) adsorption.

Model	Parameter	MBC	NaOH-MBC	Fe@NaOH-MBC
Langmuir	q_{max} (mg/g)	14.44	84.66	123.85
	K_L (L/mg)	0.145	0.084	0.158
	R^2	0.981	0.990	0.990
Freundlich	K_F (L/mg)	4.147	17.631	30.487
	1/n	0.232	0.290	0.272
	R^2	0.940	0.900	0.889

Figure 7a–i show that the adsorption capacity of all nine types of biochar for Cd(II) exhibited a rapid increasing trend with rising initial Cd^{2+} concentrations, demonstrating high adsorption rates under these conditions. At low initial concentrations, all heavy metal ions in the solution can react with the active sites and functional groups on the biochar. However, as the initial concentration continues to increase, the number of available active sites and functional groups on the biochar surface gradually decreases until they are completely utilized.

Tables 6–8 show that both the Langmuir and the Freundlich equations can adequately fit the adsorption data of the nine types of biochar. Comparing the two models, the Langmuir model consistently exhibits a higher R^2 value, indicating that the Langmuir model better describes the adsorption process. This suggests that the adsorption of Cd^{2+} by SBC, NaOH-SBC, Fe@NaOH-SBC, MBC, NaOH-MBC, Fe@NaOH-MBC, HBC, NaOH-HBC, and Fe@NaOH-HBC all follow a monolayer adsorption mechanism [60]. By comparing the Langmuir model qmax parameters of the nine carbon materials, we observe that alkali–Fe-modified carbons (Fe@NaOH-SBC, Fe@NaOH-MBC, Fe@NaOH-HBC) > NaOH-modified carbons (NaOH-SBC, NaOH-MBC, NaOH-HBC) > pristine carbons (SBC, MBC, HBC), indicating that composite modification with NaOH and $FeCl_3 \cdot 6H_2O$ significantly increases the number of adsorption sites on the biochar surface, thereby greatly enhancing its maximum Cd^{2+} adsorption capacity. Furthermore, a synergistic effect exists between iron oxide loading and alkali modification, yielding superior results compared with alkali modification alone.

Meanwhile, the Freundlich model also exhibited satisfactory fitting for the Cd(II) isothermal adsorption data for all nine biochars, with correlation coefficients (R^2) exceeding 0.8. According to literature reports, the parameter 1/n in the Freundlich model reflects both the adsorption intensity and the surface heterogeneity of the adsorbent. When $0.1 < 1/n < 1$, the adsorption process is considered favorable and easily accessible. Table 4 shows that all nine biochars displayed active and efficient heavy metal adsorption performance, confirming the high effectiveness of the materials developed in this study and highlighting their promising potential for pollutant removal in aqueous systems.

3.2.3. Adsorption Thermodynamics

Environmental temperature is a critical factor that influences the adsorption behavior of biochar. In this study, thermodynamic adsorption experiments were conducted at three temperatures (298, 308, and 318 K) to investigate the adsorption of Cd(II) on Fe@NaOH-SBC, Fe@NaOH-HBC, and Fe@NaOH-MBC. Thermodynamic parameters were analyzed by plotting ln K (where $K = q_e/C_e$) against 1/T (Figure 8). The enthalpy change (ΔH°) and entropy change (ΔS°) were obtained from the slope and intercept of the linear regression, respectively, while the Gibbs free energy change (ΔG°) was calculated using Equations (S5) and (S6). The corresponding thermodynamic parameters are summarized in Table 9.

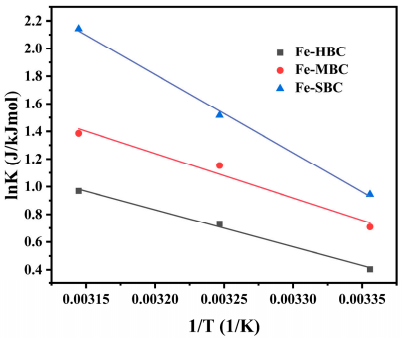

Figure 8. Influence of different temperatures on Cd(II) adsorption.

Table 9. Thermodynamic fitting parameters of Cd(II) adsorption by Fe@NaOH-SBC, Fe@NaOH-HBC, and Fe@NaOH-MBC.

T	Parameter	Fe-SBC	Fe-HBC	Fe-MBC
298	ln K (L/mol)	0.944	0.405	0.708
	ΔG° (kJ/mol)	−2.34	−1.005	−1.755
308	ln K (L/mol)	1.516	0.731	1.153
	ΔG° (kJ/mol)	−3.883	−1.872	−2.952
318	ln K (L/mol)	2.143	0.969	1.386
	ΔG° (kJ/mol)	−5.665	−2.563	−3.665
298–318	ΔS° (kJ·(mol/K))	0.166	0.078	0.096
	ΔH° (kJ/mol)	47.193	22.248	26.790
	R^2	0.998	0.995	0.975

The figure illustrates the adsorption capacity and efficiency of Fe@NaOH-SBC, Fe@NaOH-HBC, and Fe@NaOH-MBC at different temperatures. As the temperature increased from 298 to 318, the Cd(II) adsorption capacities of all three biochars showed a noticeable increase.

To further evaluate the effect of temperature on Cd(II) adsorption, the thermodynamic parameters—Gibbs free energy change (ΔG°), enthalpy change (ΔH°), and entropy change (ΔS°)—for Cd(II) adsorption on Fe@NaOH-SBC, Fe@NaOH-HBC, and Fe@NaOH-MBC were calculated based on thermodynamic principles (Table 9). The calculated ΔG° values were negative over the entire temperature range investigated, indicating that the adsorption process is thermodynamically favorable under standard-state conditions [61,62]. Moreover, ΔG° became more negative with increasing temperature (e.g., from −2.34 to −5.67 kJ·mol^{-1} for Fe-SBC as the temperature increased from 298 to 318 K), demonstrating an enhanced thermodynamic driving force at elevated temperatures [63]. This trend can be understood through the fundamental relationship $\Delta G^\circ = \Delta H^\circ - T\Delta S^\circ$. All ΔH° values are positive (22.25–47.19 kJ/mol), indicating that the adsorption process is dominated by endothermic chemical interactions [64], such as the coordination between Cd(II) and Fe-O/OH groups

on the biochar surface, ion exchange, or precipitation [65]. Among these, Fe@NaOH-HBC exhibits the highest ΔH° (47.19 kJ/mol), consistent with literature reports stating that highly efficient iron-based materials require overcoming higher energy barriers in chemical reactions [66]. This may stem from the higher-energy adsorption sites generated by the synergistic modification of NaOH and Fe [67]. This synergistic modification mechanism has been demonstrated in related studies to effectively introduce abundant surface ferric-oxy functional groups, thereby significantly enhancing the chemical adsorption capacity for heavy metals. Furthermore, $\Delta S^{\circ} > 0$ is a common thermodynamic feature in Cd(II) adsorption. The relatively low entropy values shown in Table 9 indicate that this process maintains the relative regularity of Cd(II) on the polymer surface [63].

3.3. Remediation of Cd(II) in Soil

3.3.1. Effects of Alkali–Fe-Modified Biochar Application on Soil pH, SOM, and CEC

The treatment groups in the soil pH, SOM, and CEC studies all utilized alkali–Fe-modified carbon (Fe@NaOH-SBC, Fe@NaOH-HBC, Fe@NaOH-MBC) added to the soil at different rates (1%, 3%, 5%). CK represents the soil control group without carbon addition.

Soil pH is a critical factor influencing the binding forms of heavy metals. An increase in pH can alter the surface activity of solid-phase substances in soil and enhance electrostatic attraction to heavy metal ions, thereby reducing their mobility and bioavailability [68]. Moreover, soil pH strongly affects the speciation, transport, and transformation of heavy metals [69]. The effects of different Fe@NaOH-SBC, Fe@NaOH-HBC, and Fe@NaOH-MBC treatments on the soil pH are presented in Figure 9a–c. Compared with CK, adding alkaline-iron-modified carbon at different doses to soil resulted in increased pH values, with the magnitude of pH increase positively correlated with the dose. Combined with the aforementioned XPS and XRD characterization results, the pH increase stems from the combined effects of the hydrolysis of alkaline substances introduced by NaOH modification and the deprotonation reactions of abundant oxygen-containing functional groups (e.g., -COOH, -OH) on the modified biochar surface within the soil environment. This significantly enhances the electrostatic adsorption capacity of the entire system toward positively charged Cd^{2+} ions. In addition, Fe@NaOH-SBC, Fe@NaOH-HBC, and Fe@NaOH-MBC are inherently alkaline materials. When incorporated into the soil, their alkaline components are gradually released, neutralizing the soil acidity and consequently raising the pH [70]. The elevation in soil pH promotes the formation of precipitates such as hydroxides and carbonates, which enhance the stability of heavy metals. Therefore, applying these biochars to acidic soils not only mitigates soil acidity but also reduces Cd(II) mobility and bioavailability through pH-induced immobilization mechanisms [71].

SOM interferes with heavy metal incorporation into soil, reducing the heavy metal bioavailability and toxicity [72]. Figure 9d–f show that the applications of 1%, 3%, and 5% Fe@NaOH-SBC, Fe@NaOH-HBC, and Fe@NaOH-MBC significantly increased the soil SOM content. This is primarily because biochar itself consists of highly aromatic stable carbon, and its application directly enriches the soil's inert organic carbon pool [73]. Adding biochar to soil markedly increases the SOM content due to its high carbon content, consistent with the findings of this study.

Figure 9g–i show that the applications of 1%, 3%, and 5% Fe@NaOH-SBC, Fe@NaOH-HBC, and Fe@NaOH-MBC significantly increased the soil CEC content. This is attributed to biochar's inherent richness in stable organic carbon, whose addition directly elevated the SOM. The core component of SOM—humic substances—carries abundant negative charges on its surface. Concurrently, Fe@NaOH-SBC, Fe@NaOH-HBC, and Fe@NaOH-MBC possess rich functional groups (e.g., carboxyl groups $-COO^{-}$). These negative charges serve as key sites for adsorbing and retaining cationic nutrients (e.g., K^{+}, NH_4^{+}, Ca^{2+}). Consequently,

increased SOM leads to an enhanced soil cation exchange capacity (CEC). This elevated CEC strengthens the soil's ability to immobilize Cd^{2+} through ion exchange mechanisms.

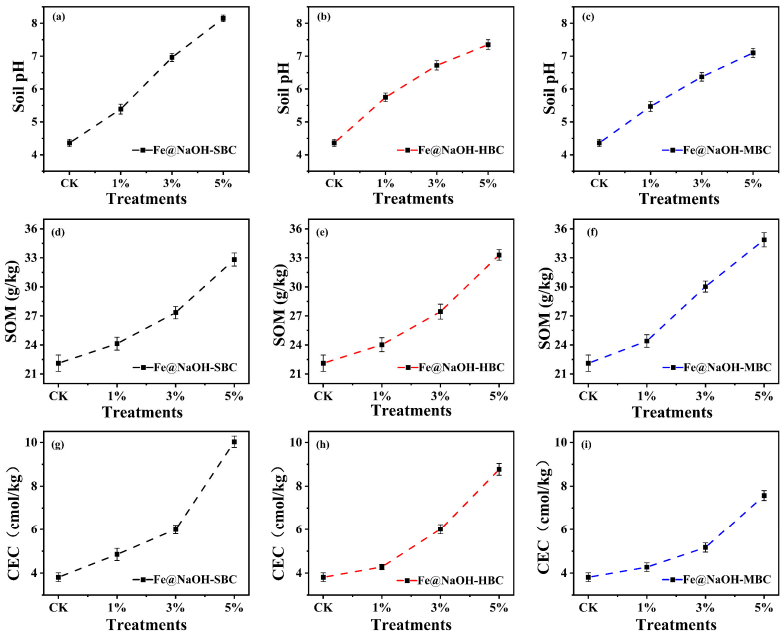

Figure 9. Effects of Fe@NaOH-SBC (**a**,**d**,**g**), Fe@NaOH-HBC (**b**,**e**,**h**), and Fe@NaOH-MBC (**c**,**f**,**i**) at different application rates on soil pH, SOM, and CEC (1%, 3%, 5%: alkaline-iron-modified biochar addition levels).

3.3.2. Effect of Applying Alkali–Fe-Modified Biochar on the Bioavailability of Heavy Metals in Soil

The available cadmium content in soil reflects its mobility and transformation potential and serves as the primary source of Cd(II) uptake by plants. The DTPA–TEA extraction method was used to determine the available Cd(II) content, providing an effective indicator of Cd(II) bioavailability in soil.

As shown in Figure 10, compared with the control group, the addition of the iron-modified biochar significantly reduced the available Cd(II) content after a 30-day incubation period. The reduction effect was dose-dependent: at a lower application rate (1%), the available Cd(II) content decreased by 13.34–16.97%, whereas at higher rates (3–5%), the reduction increased to 18.38–33.94%. These results clearly demonstrate that the available Cd(II) concentration declined progressively with increasing biochar dosage.

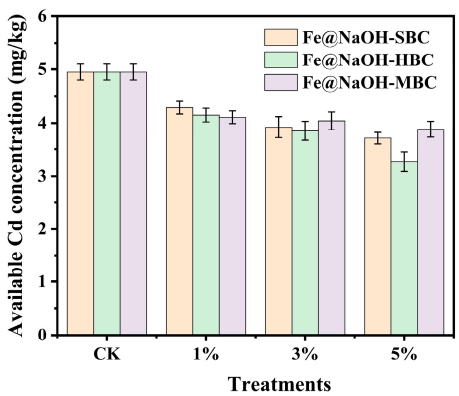

Figure 10. Shows the available Cd(II) content in soil after treatment with Fe@NaOH-SBC, Fe@NaOH-HBC, and Fe@NaOH-MBC at different addition rates (1%, 3%, 5%).

The applications of Fe@NaOH-SBC, Fe@NaOH-HBC, and Fe@NaOH-MBC effectively reduced the bioavailability of heavy metals in soil. This can be attributed to the abundant oxygen-containing functional groups on the biochar surfaces [74], which interact with Cd(II) to form stable organo-metallic complexes, thereby decreasing Cd(II) bioavailability [75]. In addition, the incorporation of these biochar-modified soil physicochemical properties—particularly by increasing pH and EC—promotes cadmium precipitation and enhances its adsorption onto biochar surfaces, ultimately reducing the Cd(II) mobility in the soil environment [76].

A negative correlation was observed between the soil pH/EC and available Cd(II) content. Soil pH plays a critical role in controlling heavy metal speciation: higher pH enhances the surface activity of solid-phase components and strengthens electrostatic attraction toward heavy metal ions, thereby decreasing their mobility. The three biochars used in this study are inherently alkaline and contain substantial amounts of ash and organic matter. Their incorporation effectively elevated soil pH and significantly reduced the available Cd(II) content, highlighting their strong potential for immobilizing heavy metals in contaminated soils.

3.3.3. Effects of Alkali–Fe-Modified Biochar on the Distribution of Heavy Metal Speciation in Soil

Previous research has demonstrated that the biotoxicity and bioaccumulation potential of heavy metals in organisms are determined by their chemical speciation and bioavailability rather than by their total concentrations alone [77]. Therefore, in addition to analyzing the available Cd(II) fraction, this study employed the Tessier sequential extraction procedure to investigate the detailed distribution of cadmium (Cd) chemical species. The concentrations of Cd(II) species in soils treated with different application rates of Fe@NaOH-SBC, Fe@NaOH-HBC, and Fe@NaOH-MBC are presented in Figure 11.

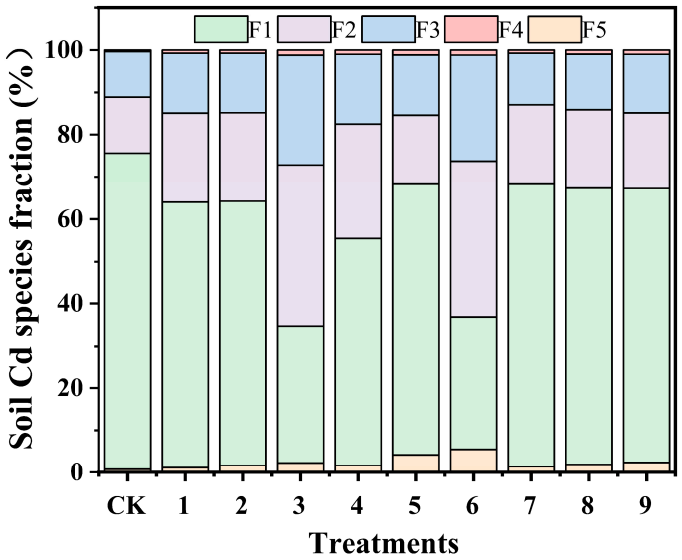

Figure 11. Shows the distribution of heavy metal speciation in soils treated with Fe@NaOH-SBC, Fe@NaOH-HBC, and Fe@NaOH-MBC at different additive concentrations. Labeled treatment groups: CK and 1–9 correspond to the cadmium-containing clay control group without carbon addition (CK) and those treated with Fe@NaOH-SBC at 1% (1), 3% (2), and 5% (3); Fe@NaOH-HBC at 1% (4), 3% (5), and 5% (6); and Fe@NaOH-MBC at 1% (7), 3% (8), and 5% (9).

The Tessier method [26], which is widely applied for heavy metal speciation analysis in soils, classifies metals into five operationally defined fractions according to their bioactivity: exchangeable (F1), carbonate-bound (F2), Fe–Mn-oxide-bound (F3), organic-matter-bound

(F4), and residual (F5). As shown in Figure 11, in the untreated soil, Cd(II) was primarily present in the exchangeable fraction (F1), accounting for 74.882% of the total. After a 30-day incubation period, the proportion of F1 decreased to between 31.384% and 66.913% across all treatment groups. Concurrently, the proportion of F2 increased from 13.283% to 16.353–38.105%, F3 increased from 10.792% to 12.200–26.008%, F4 increased from 0.332% to 0.723–1.128%, and F5 increased from 0.710% to 1.077–5.458%.

The reduction in the exchangeable fraction (F1) can be attributed to the alkaline properties of Fe@NaOH-SBC, Fe@NaOH-HBC, and Fe@NaOH-MBC, which increased the concentrations of OH^- and CO_3^{2-} in the soil, thereby promoting the formation of insoluble Cd(II) hydroxides and carbonates [78]. The increase in the carbonate-bound fraction (F2), which is highly sensitive to soil pH, corresponded with the observed rise in the pH. The increases in the organic-matter-bound (F4) and residual (F5) fractions were associated with the abundant surface functional groups of the biochar and the precipitation of Cd(II) with CO_3^{2-} and other anions [79]. Furthermore, mineral components within the biochar facilitated the transformation of Cd(II) into more stable residual forms through adsorption, complexation, and precipitation processes [80]. The residual fraction represents the most stable form of heavy metals, exhibiting minimal bioavailability and posing a low risk for plant uptake. Notably, beyond the pH-driven precipitation and adsorption mechanisms described above, the Cd immobilization effect of iron-modified biochar is likely closely linked to the soil iron redox cycle it triggers. Recent studies indicate that iron-modified biochar (e.g., modified with $Fe(NO_3)_3$ or $Fe_2(SO_4)_3$) can function as an electron shuttle, significantly promoting the reduction in Fe(III) and the reoxidation of Fe(II) in soil [81]. This dynamic iron cycle offers multiple environmental benefits: First, the reoxidation of Fe(II) generates abundant, highly reactive amorphous iron oxides (e.g., goethite) with large specific surface areas. These provide abundant specific adsorption sites for Cd, significantly promoting its conversion to iron–manganese-oxide-bound Cd (F3) [82]. This finding strongly correlates with the observed substantial increase in the proportion of F3 (Fe–Mn-oxide-bound) in this study. Second, the iron-cycling process itself can drive the co-precipitation or mineral-phase encapsulation of coexisting heavy metals, further enhancing their long-term stability. Therefore, the Cd stabilization achieved by iron-modified biochar in this study results from the combined effects of "pH-induced precipitation/adsorption" and "iron redox cycling-mediated specific adsorption and mineral transformation".

Overall, the increase in soil pH was identified as the primary mechanism driving the transformation of Cd(II) species [83]. Compared with the control, all application rates of Fe@NaOH-SBC, Fe@NaOH-HBC, and Fe@NaOH-MBC effectively promoted the conversion of the labile F1 fraction into the more stable and less bioavailable fractions (F2, F3, F4, and F5). The conversion efficiency increased significantly with higher biochar application rates. These findings confirm that the biochar developed in this study is highly effective at immobilizing Cd(II) in contaminated soils.

3.3.4. Effects of Alkali–Fe-Modified Biochar on the Spinach Seed Germination Experiment

We conducted germination experiments by adding spinach seeds to soil that had been passivated for 30 days. The results are shown in Table 10. Compared with healthy soil, the cadmium-contaminated control (CK) caused a significant delay in germination time to day 9 and a sharp drop in the emergence rate to 40%, confirming the strong inhibition of seed physiological processes by high concentrations of available cadmium. All biochar treatments alleviated this toxicity to varying degrees, exhibiting a dose-dependent pattern of initial improvement followed by diminishing returns. Notably, the remediation effect peaked at the 3% addition rate rather than 5%. For instance, at a 3% Fe@NaOH-SBC addition, the emergence rate (80%) and germination time (day 5) approached healthy soil

levels; however, increasing the addition to 5% reduced the emergence to 50% and delayed germination to day 10.

Table 10. Spinach seed germination experiment after treating cadmium-contaminated soil with Fe@NaOH-SBC, Fe@NaOH-HBC, and Fe@NaOH-MBC at different addition levels (1%, 3%, 5%).

Treatments	Germination Time	Emergence Rate
Healthy soil	Day 5	90%
Cd-contaminated soil	Day 9	40%
Fe@NaOH-SBC 1%	Day 9	45%
Fe@NaOH-SBC 3%	Day 5	80%
Fe@NaOH-SBC 5%	Day 10	50%
Fe@NaOH-HBC 1%	Day 8	45%
Fe@NaOH-HBC 3%	Day 6	75%
Fe@NaOH-HBC 5%	Day 7	60%
Fe@NaOH-MBC 1%	Day 9	45%
Fe@NaOH-MBC 3%	Day 6	75%
Fe@NaOH-MBC 5%	Day 7	55%

4. Conclusions

In this study, three types of alkali-iron composite-modified biochar were successfully prepared and systematically evaluated, confirming their potential as highly efficient, multifunctional remediation materials with outstanding application prospects in both cadmium-contaminated water bodies and soil environments. Through comprehensive cross-medium (water–soil–plant) validation, this study elucidated the microscopic mechanisms underlying its high-efficiency remediation and revealed the macroscopic principle of "moderate remediation" in practical soil applications. This provides crucial theoretical foundations and technical solutions for the precise and safe remediation of cadmium-contaminated environments.

Through composite modification with NaOH and $FeCl_3 \cdot 6H_2O$, an iron oxide (Fe_3O_4/α-FeOOH) carrier material was successfully developed, featuring a high specific surface area, abundant pore structure, and numerous surface functional groups. Batch adsorption experiments confirmed that the adsorption process is primarily governed by chemical adsorption mechanisms, including surface ion exchange and complexation with iron oxides and oxygen-containing functional groups. After 30 days of application to cadmium-contaminated soil, the composites significantly increased the soil pH, organic matter content, and cation exchange capacity. These changes collectively promoted the transformation of cadmium from highly bioavailable exchangeable forms to more stable species, markedly reducing the available cadmium levels. Spinach seed germination tests further validated the remediation efficacy from a biological perspective. The results indicate that a 3% addition adjusted the soil pH to the near-neutral optimal range, achieving an optimal plant response, whereas a 5% addition risked alkaline stress due to excessive pH elevation. This clearly established the practical principle of "moderate neutralization."

Alkali-iron-modified carbon demonstrates integrated "water–soil" application potential, ranging from the purification of contaminated water to the safe remediation of polluted soils. Through synergistic mechanisms—including pH elevation, increased SOM, and enhanced CEC—it efficiently stabilizes cadmium in soil and ultimately ensures safe plant germination by reducing its bioavailability. This study recommends a 3% Fe@NaOH-SBC addition rate as the optimal remediation strategy for this contaminated soil condition.

Based on the above properties, this material exhibits clear application potential. It can be used as a soil conditioner for the remediation of mildly to moderately Cd-contaminated acidic farmland (recommended application rate: 3%) to ensure the safe production of

leafy vegetables. In addition, it can serve as an adsorbent matrix for the treatment of low-concentration Cd-containing agricultural wastewater (e.g., <50 mg L^{-1}), enabling advanced purification.

However, this study has certain limitations, and the practical effectiveness of the material still requires further validation in future work. The remediation performance was evaluated only under a specific soil type (purple soil) and a single contamination level (6 mg kg^{-1}), and thus the material's universality across different soil environments and pollution gradients remains to be assessed. The adsorption experiments were primarily carried out in a single-solute Cd(II) system. Preliminary competitive adsorption tests suggest that coexisting ions (e.g., Ca^{2+}, Mg^{2+}, Pb^{2+}) may decrease Cd fixation efficiency due to competition for adsorption sites. The long-term stability of the remediation effect (e.g., under leaching and aging processes) and the economic feasibility of field-scale applications have not yet been systematically investigated.

Therefore, future research will focus on the following directions: Systematically evaluating and enhancing the selective adsorption performance of the material in multi-ion coexistence systems and real environmental media (e.g., contaminated water bodies, soil leachates); assessing the long-term environmental stability of immobilized cadmium through extended leaching and aging experiments; conducting a full-chain cost–benefit analysis to provide economic and feasibility evidence for the engineering-scale application of this technology.

Supplementary Materials: The following supporting information can be downloaded at: https://www.mdpi.com/article/10.3390/su18010373/s1.

Author Contributions: X.Z.: conceptualization, investigation, data curation, formal analysis, writing—original draft, methodology, software; D.S.: resources, funding acquisition; Y.X.: investigation; J.L.: methodology; J.N., G.Y., H.C. and T.X.: data curation. All authors have read and agreed to the published version of the manuscript.

Funding: This study was financially sponsored by the Science and Technology Research Program of Chongqing University of Arts and Sciences (Grant No. P2021YL12) and the Scientific and Technological Research Program of Chongqing Municipal Education Commission (Grant No. KJZD-K202301305).

Institutional Review Board Statement: Not applicable.

Informed Consent Statement: Not applicable.

Data Availability Statement: All data are included in the article.

Conflicts of Interest: The authors declare no conflicts of interest.

References

1. Ahmad, Z.; Gao, B.; Mosa, A.; Yu, Z.; Yin, Y.; Bashir, A.; Ghoveisi, H. Removal of Cu(II), Cd(II) and Pb(II) Ions from Aqueous Solutions by Biochar Derived from Potassium-Rich Biomass. *J. Clean. Prod.* **2018**, *180*, 437–449. [CrossRef]
2. Huang, X.; Zhao, H.; Zhang, G.; Li, J.; Ji, P.; Liu, Y. Potential of Removing Cd(II) and Pb(II) from Contaminated Water Using a Newly Modified Fly Ash. *Chemosphere* **2020**, *242*, 125148. [CrossRef]
3. Fei, X.; Lou, Z.; Xiao, R.; Ren, Z.; Lv, X. Source Analysis and Source-Oriented Risk Assessment of Heavy Metal Pollution in Agricultural Soils of Different Cultivated Qualities. *J. Clean. Prod.* **2022**, *341*, 130942. [CrossRef]
4. Purkayastha, D.; Mishra, U.; Biswas, S. A Comprehensive Review on Cd(II) Removal from Aqueous Solution. *J. Water Process Eng.* **2014**, *2*, 105–128. [CrossRef]
5. Liang, L.; Li, X.; Lin, Z.; Su, X.; Tian, Y. The Removal of Cd by Sulfidated Nanoscale Zero-Valent Iron: The Structural, Chemical Bonding Evolution and the Reaction Kinetics. *Chem. Eng. J.* **2020**, *382*, 122933. [CrossRef]
6. Wang, Z.; Lin, Z.; Li, Y.; Li, Y.; Luo, J.; Wu, Y.; Ye, Z.; Huang, Y.; Li, F. Diffusive Gradient in Thin Films Combined with Machine Learning to Discern the Accumulation Characteristics and Driving Factors of Cd and Cu in Soil-Rice Systems. *J. Hazard. Mater.* **2025**, *495*, 138924. [CrossRef]

7. Sun, C.; Chen, T.; Huang, Q.; Wang, J.; Lu, S.; Yan, J. Enhanced Adsorption for Pb(II) and Cd(II) of Magnetic Rice Husk Biochar by $KMnO_4$ Modification. *Environ. Sci. Pollut. Res.* **2019**, *26*, 8902–8913. [CrossRef]
8. Hamid, Y.; Tang, L.; Sohail, M.I.; Cao, X.; Hussain, B.; Aziz, M.Z.; Usman, M.; He, Z.L.; Yang, X. An Explanation of Soil Amendments to Reduce Cadmium Phytoavailability and Transfer to Food Chain. *Sci. Total Environ.* **2019**, *660*, 80–96. [CrossRef]
9. Zhang, L.; Guo, J.; Huang, X.; Wang, W.; Sun, P.; Li, Y.; Han, J. Functionalized Biochar-Supported Magnetic $MnFe_2O_4$ Nanocomposite for the Removal of Pb(II) and Cd(II). *RSC Adv.* **2019**, *9*, 365–376. [CrossRef] [PubMed]
10. Leng, L.; Xiong, Q.; Yang, L.; Li, H.; Zhou, Y.; Zhang, W.; Jiang, S.; Li, H.; Huang, H. An Overview on Engineering the Surface Area and Porosity of Biochar. *Sci. Total Environ.* **2021**, *763*, 144204. [CrossRef] [PubMed]
11. Zhang, R.H.; Xie, Y.; Zhou, G.; Liu, J.; Liu, F.; Huang, H. The Effects of Short-Term, Long-Term, and Reapplication of Biochar on the Remediation of Heavy Metal-Contaminated Soil. *Ecotoxicol. Environ. Saf.* **2022**, *248*, 114316. [CrossRef]
12. Xu, H.; Ou, Z.; Li, W.; Hu, T.; Zhang, Y.; Xu, H.; Wang, J.; Li, Y. Cadmium(II) Adsorption by Recyclable Zeolite-Loaded Hydrogel: Extension to the Removal of Cadmium(II) from Contaminated Soil. *J. Hazard. Mater.* **2024**, *445*, 130532. [CrossRef]
13. Wang, L.; Wang, Y.J.; Ma, F.; Tankpa, V.; Bai, S.; Guo, X.; Wang, X. Mechanisms and Reutilization of Modified Biochar Used for Removal of Heavy Metals from Wastewater: A Review. *Sci. Total Environ.* **2019**, *668*, 1298–1309. [CrossRef] [PubMed]
14. Fu, H.; Ma, S.; Xu, S.; Duan, R.; Cheng, G.; Zhao, P. Hierarchically Porous Magnetic Biochar as an Efficient Amendment for Cadmium in Water and Soil: Performance and Mechanism. *Chemosphere* **2021**, *281*, 130990. [CrossRef]
15. Irshad, M.K.; Chen, C.; Noman, A.; Ibrahim, M.; Adeel, M.; Shang, J. Goethite-Modified Biochar Restricts the Mobility and Transfer of Cadmium in Soil-Rice System. *Chemosphere* **2020**, *242*, 125152. [CrossRef] [PubMed]
16. Zhang, J.Y.; Zhou, H.; Gu, J.F.; Huang, F.; Yang, W.J.; Wang, S.L.; Yuan, T.Y.; Liao, B.H. Effects of Nano-Fe_3O_4-Modified Biochar on Iron Plaque Formation and Cd Accumulation in Rice (*Oryza sativa* L.). *Environ. Pollut.* **2020**, *260*, 113970. [CrossRef]
17. Islam, M.S.; Chen, Y.L.; Weng, L.P.; Ma, J.; Khan, Z.H.; Cheng, D.; Li, Y.C. Watering Techniques and Zero-Valent Iron Biochar pH Effects on As and Cd Concentrations in Rice Rhizosphere Soils, Tissues and Yield. *J. Environ. Sci.* **2021**, *100*, 144–157. [CrossRef] [PubMed]
18. Wan, X.M.; Li, C.Y.; Parikh, S.J. Simultaneous Removal of Arsenic, Cadmium, and Lead from Soil by Iron-Modified Magnetic Biochar. *Environ. Pollut.* **2020**, *261*, 114157. [CrossRef]
19. Wang, S.S.; Zhao, M.Y.; Zhou, M.; Li, Y.C.; Wang, J.; Gao, B.; Sato, S.; Feng, K.; Yin, W.; Igalavithana, A.D.; et al. Biochar-Supported nZVI (nZVI/BC) for Contaminant Removal from Soil and Water: A Critical Review. *J. Hazard. Mater.* **2019**, *373*, 820–834. [CrossRef]
20. Ghazoui, M.; Elkacmi, R.; Sylla, A.S.; Anter, N.; Dabali, S.; Boudouch, O. Innovative adsorbents and mechanisms for radionuclide removal from aqueous nuclear waste: A comprehensive review of materials, performance, and future perspectives. *Total Environ. Eng.* **2025**, *5*, 100042. [CrossRef]
21. Li, H.; Dong, X.; Da Silva, E.B.; De Oliveira, L.M.; Chen, Y.; Ma, L.Q. Mechanisms of Metal Sorption by Biochar: Biochar Characteristics and Modifications. *Chemosphere* **2017**, *178*, 466–478. [CrossRef]
22. Wang, J.; Kang, Y.; Duan, H.; Zhou, Z.; Li, Y.; Wang, H.; Li, Y. Remediation of Cd(II) in Aqueous Systems by Alkali-Modified (Ca) Biochar and Quantitative Analysis of Its Mechanism. *Arab. J. Chem.* **2022**, *15*, 103750. [CrossRef]
23. Hossain, M.A.; Ngo, H.H.; Guo, W.S.; Nghiem, L.D.; Hai, F.I.; Vigneswaran, S.; Nguyen, T.V. Competitive Adsorption of Metals on Cabbage Waste from Multi-Metal Solutions. *Bioresour. Technol.* **2014**, *160*, 79–88. [CrossRef]
24. Fan, J.; Cai, C.; Chi, H.; Reid, B.J.; Coulon, F.; Zhang, Y.; Hou, Y. Remediation of Cadmium and Lead Polluted Soil Using Thiol-Modified Biochar. *J. Hazard. Mater.* **2020**, *388*, 122037. [CrossRef] [PubMed]
25. *HJ/T 166-2004*; The Technical Specification for Soil Environmental Monitoring. Ministry of Ecology and Environment: Beijing, China.
26. Tessier, A.P.; Campbell, P.G.C.; Bisson, M. Sequential Extraction Procedure for the Speciation of Particulate Trace Metals. *Anal. Chem.* **1979**, *51*, 844–851. [CrossRef]
27. Al-Wabel, M.I.; Al-Omran, A.; El-Naggar, A.H.; Nadeem, M.; Usman, A.R. Pyrolysis temperature induced changes in characteristics and chemical composition of biochar poduced from conocarpus wastes. *Bioresour. Technol.* **2013**, *131*, 374–379. [CrossRef]
28. Ahmad, M.; Lee, S.S.; Dou, X.; Mohan, D.; Sung, J.K.; Yang, J.E.; Ok, Y.S. Effects of pyrolysis temperature on soybean stover- and peanut shell-derived biochar properties and TCE adsorption in water. *Bioresour. Technol.* **2012**, *118*, 536–544. [CrossRef]
29. Xu, S.; Yu, W.; Liu, S.; Wu, J.; Huang, S.; Yang, J.; Gao, Y. Adsorption of Hexavalent Chromium Using Banana Pseudostem Biochar and Its Mechanism. *Sustainability* **2018**, *10*, 4250. [CrossRef]
30. Ahmad, Z.; Gao, B.; Mosa, A.; Yu, Z.; Yin, Y.; Bashir, A.; Ghoveisi, H. Adsorption Properties and Mechanism of Suaeda Biochar and Modified Materials for Tetracycline. *Environ. Res.* **2023**, *235*, 116549. [CrossRef]
31. Zhu, H.; Li, J.; Wu, D.; Zhang, G.; Sun, Y.; Wang, A.; Sun, K. Construction of the Hierarchical Porous Biochar with an Ultrahigh Specific Surface Area for Application in High-Performance Lithium-Ion Capacitor Cathode. *Biochar* **2023**, *5*, 46. [CrossRef]

32. Nguyen, V.T.; Nguyen, T.B.; Huang, C.P.; Chen, C.W.; Bui, X.T.; Dong, C.D. Alkaline Modified Biochar Derived from Spent Coffee Ground for Removal of Tetracycline from Aqueous Solutions. *J. Water Process Eng.* **2021**, *40*, 101908. [CrossRef]
33. Shen, Z.; Zhang, Y.; Jin, F.; McMillan, O.; Al-Tabbaa, A. Qualitative and Quantitative Characterisation of Adsorption Mechanisms of Lead on Four Biochar. *Sci. Total Environ.* **2017**, *609*, 1401–1410. [CrossRef]
34. Zhang, H.; Yang, J.; Deng, Y.; Li, Y.; Wang, J.; Wang, L.; Wang, W. αFeOOH@HTC with abundant oxygen vacancy enhances the adsorption of As(III) in different phosphate environments. *J. Environ. Chem. Eng.* **2024**, *12*, 111776. [CrossRef]
35. Zhang, S.; Yang, X.; Liu, L.; Ju, M.; Zheng, K. Adsorption Behavior of Selective Recognition Functionalized Biochar to Cd(II) in Wastewater. *Materials* **2018**, *11*, 299. [CrossRef]
36. Chen, B.; Zhou, D.; Zhu, L. Transitional Adsorption and Partition of Nonpolar and Polar Aromatic Contaminants by Biochar of Pine Needles with Different Pyrolytic Temperatures. *Environ. Sci. Technol.* **2008**, *42*, 5137–5143. [CrossRef]
37. Yu, C.; Zhang, Z.; Yang, I.; Liu, Y.; Wang, Y.; Zhang, L.; Peng, H. Glucose Enhanced the Oxidation Performance of Iron-Manganese Binary Oxides: Structure and Mechanism of Removing Tetracycline. *J. Colloid Interface Sci.* **2020**, *573*, 287–298. [CrossRef]
38. Zeng, L.; Luo, D.; Liu, L.; Huang, X.; Liu, Y.; Wei, L.; Xiao, T.; Wu, Q. Alkali/Fe-Modified Biochar for Cd-As Contamination in Water and Soil: Performance and Mechanism. *Environ. Technol. Innov.* **2023**, *32*, 103381. [CrossRef]
39. Uchimiya, M.; Lima, I.M.; Klasson, K.T.; Wartelle, L.H. Textural and Chemical Properties of Swine-Manure-Derived Biochar Pertinent to Its Potential Use as a Soil Amendment. *Chemosphere* **2012**, *89*, 198–203. [CrossRef]
40. Lin, B.F.; Chen, Z.H.; Yang, F.L.; Wang, Y.; Li, X.; He, Y. Adsorption Performance of Tetracycline by Manganese Ferrite-Modified Biochar. *J. Agro-Environ. Sci.* **2023**, *42*, 1585–1596.
41. Choi, H.; Al-Abed, S.R.; Agarwal, S.; Dionysiou, D.D. Synthesis of Reactive Nano-Fe/Pd Bimetallic System-Impregnated Activated Carbon for the Simultaneous Adsorption and Dechlorination of PCBs. *Chem. Mater.* **2008**, *20*, 3649–3655. [CrossRef]
42. Wu, J.; Huang, D.; Liu, X.; Meng, J.; Tang, C.; Xu, J. Remediation of as(iii) and cd(ii) co-contamination and its mechanism in aqueous systems by a novel calcium-based magnetic biochar. *J. Hazard. Mater.* **2018**, *348*, 10–19. [CrossRef]
43. Zahid, M.; Yaqub, M.; Nawaz, H.; Latif, M.; Anjum, M.N.; Nawaz, A.; Shahzad, M.I.; Zia, M.A.; Javaid, A.; Mahmood, K. Influence of Graphene Oxide Contents on Mechanical Behavior of Polyurethane Composites Fabricated with Different Diisocyanates. *Polymers* **2021**, *13*, 444. [CrossRef]
44. Zhongrui, L.; Zhiyong, L. Optimization of Bucky paper-enhanced Multifunctional Thermoplastic Composites. *Sci. Rep.* **2017**, *7*, 42423.
45. Kopcsik, E.; Mucsi, Z.; Schiwert, R.; Vanyorek, L.; Viskolcz, B.; Nagy, M. Aromatic pi-complexation of 1,5-diisocyanonaphthalene with benzene derivatives. *Sci. Rep.* **2025**, *15*, 629. [CrossRef]
46. Chen, Y.; Li, M.; Li, Y.; Liu, Y.; Chen, Y.; Li, H.; Li, L.; Xu, F.; Jiang, H.; Chen, L. Hydroxyapatite modified sludge-based biochar for the adsorption of Cu^{2+} and Cd^{2+}: Adsorption behavior and mechanisms. *Bioresour. Technol.* **2021**, *321*, 124413. [CrossRef]
47. Huang, X.; Kong, L.; Huang, S.; Liu, M.; Li, L. Synthesis of novel magnetic sulfur-doped Fe_3O_4 nanoparticles for efficient removal of Pb(II). *Sci. China* **2018**, *61*, 164–171. [CrossRef]
48. Ma, J.; Zhou, B.; Zhang, H.; Zhang, W. Fe/S modified sludge-based biochar for tetracycline removal from water. *Powder Technol.* **2019**, *364*, 889–900. [CrossRef]
49. Tan, W.T.; Zhou, H.; Tang, S.F.; Zeng, P.; Gu, J.F.; Liao, B.H. Enhancing cd(ii)adsorption on rice straw biochar by modification of iron and manganese oxides. *Environ. Pollut.* **2022**, *300*, 118899. [CrossRef] [PubMed]
50. Qiu, Y.; Xu, X.; Xu, Z.; Liang, J.; Yu, Y.; Cao, X. Contribution of different iron species in the iron-biochar composites to sorption and degradation of two dyes with varying properties. *Chem. Eng. J.* **2020**, *389*, 124471. [CrossRef]
51. Wang, B.; Ye, C.; Li, F.Y.; Liu, J.; Zhang, Q. Studies on Adsorption of Nitrate from Modified Hydrophyte Biochar. *China Environ. Sci.* **2017**, *37*, 116–122.
52. Tang, L.; Yu, J.; Pang, Y.; Zeng, G.; Deng, Y.; Wang, J.; Ren, X.; Ye, S.; Peng, B.; Feng, H. Sustainable efficient adsorbent: Alkali-acid modified magnetic biochar derived from sewage sludge for aqueous organic contaminant removal. *Chem. Eng. J.* **2018**, *336*, 160–169. [CrossRef]
53. Wu, W.-W.; Mao, L.; Hu, H.-L.; Gan, W.-J. Effect of Fe-bearing Modifying Agents on Adsorption Performance of Magnetic Straw-Derived Biochars for Cr(VI). *Nonferrous Met. (Extr. Metall.)* **2022**, 90–98. [CrossRef]
54. Duan, X.; Srinivasakannan, C.; Wang, X.; Wang, F.; Liu, X. Synthesis of Activated Carbon Fibers from Cotton by Microwave Induced H_3PO_4 Activation. *J. Taiwan Inst. Chem. Eng.* **2017**, *70*, 374–381. [CrossRef]
55. Cazetta, A.L.; Pezoti, O.; Bedin, K.C.; Silva, T.L.; Paesano Junior, A.; Asefa, T.; Almeida, V.C. Magnetic Activated Carbon Derived from Biomass Waste by Concurrent Synthesis: Efficient Adsorbent for Toxic Dyes. *ACS Sustain. Chem. Eng.* **2016**, *4*, 1058–1068. [CrossRef]
56. Verma, L.; Singh, J.S. Synthesis of Novel Biochar from Waste Plant Litter Biomass for the Removal of Arsenic (III and V) from Aqueous Solution: A Mechanism Characterization, Kinetics and Thermodynamics. *J. Environ. Manag.* **2019**, *248*, 109235. [CrossRef] [PubMed]

57. Gaskin, J.W.; Steiner, C.; Harris, K.; Das, K.C.; Bibens, B. Effect of Low-Temperature Pyrolysis Conditions on Biochar for Agricultural Use. *Trans. ASABE* **2008**, *51*, 2061–2069. [CrossRef]
58. Zhang, H.; Zhou, C.; Zeng, H.; Wu, H.; Yang, L.; Deng, L.; Shi, Z. ZIF-8 assisted synthesis of magnetic core-shell Fe_3O_4@CuS nanoparticles for efficient sulfadiazine degradation via H_2O_2 activation: Performance and mechanism. *J. Colloid Interface Sci.* **2021**, *594*, 502–512. [CrossRef]
59. Yang, F.; Zhang, S.; Li, H.; Li, S.; Cheng, K.; Li, J.S.; Tsang, D.C. Com straw-derived biochar impregnated with α-FeOOH nanorods for highly effective copper removal. *Chem. Eng. J.* **2018**, *348*, 191–201. [CrossRef]
60. Han, Y.; Cao, X.; Ouyang, X.; Sohi, S.P.; Chen, J. Adsorption Kinetics of Magnetic Biochar Derived from Peanut Hull on Removal of Cr(VI) from Aqueous Solution: Effects of Production Conditions and Particle Size. *Chemosphere* **2016**, *145*, 336–341. [CrossRef]
61. Huang, Y.; Gao, M.; Deng, Y.; Khan, Z.H.; Liu, X.; Song, Z.; Qiu, W. Efficient Oxidation and Adsorption of As(II)and As(V) in Water Using a Fenton-like Reagent, (Ferrihydrite)-Loaded Biochar. *Sci. Total Environ.* **2020**, *715*, 136957. [CrossRef]
62. Khan, M.I.; Nadeem, I.; Majid, A.; Shakil, M. Adsorption Mechanism of Palbociclib Anticancer Drug on Two Different Functionalized Nanotubes as a Drug Delivery Vehicle: A First Principle's Study. *Appl. Surf. Sci.* **2021**, *546*, 149129. [CrossRef]
63. Ye, S.; Zhang, W.; Hu, X.; He, H.; Zhang, Y.; Li, W.; Hu, G.; Li, Y.; Deng, X. Selective Adsorption Behavior and Mechanism for Cd(II) in Aqueous Solution with a Recoverable Magnetie-Surface Ion-Imprinted Polymer. *Polymers* **2023**, *15*, 2416. [CrossRef] [PubMed] [PubMed Central]
64. OuldM'hamed, M.; Khezami, L.; Alshammari, A.G.; Ould-Mame, S.M.; Ghiloufi, I.; Lemine, O.M. Removal of cadmium(II) ions from aqueous solution using Ni (15 wt.%)-doped α-Fe_2O_3 nanocrystals: Equilibrium, thermodynamic, and kinetic studies. *Water Sci. Technol. J. Int. Assoc. Water Pollut. Res.* **2015**, *72*, 608–615. [CrossRef]
65. Yang, T.; Xu, Y.; Huang, Q.; Sun, Y.; Liang, X.; Wang, L.; Qin, X.; Zhao, L. Adsorption characteristics and the removal mechanism of two novel Fe-Zn composite modified biochar for Cd(II) in water. *Bioresour. Technol.* **2021**, *333*, 125078. [CrossRef] [PubMed]
66. Ocon, J.D.; Tuan, T.N.; Yi, Y.; de Leon, R.L.; Lee, J.K.; Lee, J. Ultrafast and stable hydrogen generation from sodium borohydride in methanol and water over Fe–B nanoparticles. *J. Power Sources* **2013**, *243*, 444–450. [CrossRef]
67. Zheng, H.; Guo, H.; Dai, P.; Zhang, J.; Wang, D.; Faheem, M.; Liu, Z.; Tao, M. Vinasse-derived magnetic porous Fe-biochar for synergistic adsorption and non-radical oxidation of bisphenol A: Mechanisms and applications. *Environ. Res.* **2026**, *289*, 123395. [CrossRef]
68. Jing, F.; Chen, C.; Chen, X.M.; Liu, W.; Wen, X.; Hu, S.; Chen, Y. Effects of Wheat Straw Derived Biochar on Cadmium Availability in a Paddy Soil and Its Accumulation in Rice. *Environ. Pollut.* **2020**, *257*, 113592. [CrossRef]
69. Ali, A.; Guo, D.; Mahar, A.; Wang, P.; Ma, F.; Shen, F.; Li, R.; Zhang, Z. Phytoextraction of Toxic Trace Elements by Sorghum bicolor Inoculated with *Streptomyces pactum* (Act12) in Contaminated Soils. *Ecotoxicol. Environ. Saf.* **2017**, *139*, 202–209. [CrossRef] [PubMed]
70. An, X.; Wu, Z.; Yu, J.; Cravotto, G.; Liu, X.; Li, Q.; Wang, J. Copyrolysis of Biomass, Bentonite, and Nutrients as a New Strategy for the Synthesis of Improved Biochar-Based Slow-Release Fertilizers. *ACS Sustain. Chem. Eng.* **2020**, *8*, 3181–3190. [CrossRef]
71. Guo, G.Z.; Li, X.W.; Gao, M.L.; Liu, Y.; Cheng, S.; Xie, Y.; Wang, Y. Effect of Fe–Mn–Ce Modified Biochar Composite on Microbial Diversity and Properties of Arsenic-Contaminated Paddy Soils. *Chemosphere* **2020**, *250*, 126249. [CrossRef]
72. Huang, D.; Deng, R.; Wan, J.; Zeng, G.; Xue, W.; Wen, X.; Zhou, C.; Hu, L.; Liu, X.; Xu, P.; et al. Remediation of lead-contaminated sediment by biochar-supported nano-chlorapatite: Accompanied with the change of available phosphorus and organic matters. *J. Hazard. Mater.* **2018**, *348*, 109–116. [CrossRef]
73. Abdin, Y.; Usman, A.; Ok, Y.S.; Tsang, Y.F.; Al-Wabel, M. Competitive sorption and availability of coexisting heavy metals in mining-contaminated soil: Contrasting effects of mesquite and fishbone biochars. *Environ. Res.* **2020**, *181*, 108846. [CrossRef]
74. Pattnaik, B.K.; Behera, R.; Santra, S.C.; Choudhury, S.; Biswas, J.K.; Hossain, A.; Moulick, D. Potentials of Urban Waste Derived Biochar in Minimizing Heavy Metal Bioavailability: A Techno-Economic Review. *iScience* **2025**, *28*, 111915. [CrossRef] [PubMed]
75. Su, H.; Fang, Z.; Tsang, P.E.; Zheng, L.; Cheng, W.; Fang, J.; Zhao, D. Remediation of Hexavalent Chromium Contaminated Soil by Biochar-Supported Zero-Valent Iron Nanoparticles. *J. Hazard. Mater.* **2016**, *318*, 533–540. [CrossRef]
76. Wang, Y.; Zhong, B.; Shafi, M.; Ma, J.; Guo, J.; Wu, J.; Ye, Z.; Liu, D.; Jin, H. Effects of Biochar on Growth and Heavy Metals Accumulation of Moso Bamboo (*Phyllostachys pubescens*), Soil Physical Properties, and Heavy Metals Solubility in Soil. *Chemosphere* **2019**, *219*, 510–516. [CrossRef] [PubMed]
77. Morera, M.T.; Echeverría, J.C.; Mazkiarán, C.; Garrido, J.J. Isotherms and Sequential Extraction Procedures for Evaluating Sorption and Distribution of Heavy Metals in Soils. *Environ. Pollut.* **2001**, *113*, 135–144. [CrossRef] [PubMed]
78. Zhu, Q.; Wu, J.; Wang, L.; Yang, G.; Zhang, X. Effect of Biochar on Heavy Metal Speciation of Paddy Soil. *Water Air Soil Pollut.* **2015**, *226*, 429. [CrossRef]
79. Bashir, S.; Shaaban, M.; Hussain, Q.; Iqbal, J.; Khan, K.S.; Husain, A.; Ahmed, N.; Mehmood, S.; Hu, H. Influence of Organic and Inorganic Passivators on Cd and Pb Stabilization and Microbial Biomass in a Contaminated Paddy Soil. *J. Soils Sediments* **2018**, *18*, 2948–2959. [CrossRef]

80. Izadi, L.N.; Tamadoni, A.; Siebecker, M.G.; Sricharoenvech, P.; Barreto, M.S.C.; Fischel, M.H.H.; Tappero, R.; Sparks, D.L. Hurricanes and turbulent floods threaten arsenic-contaminated coastal soils and vulnerable communities. *Environ. Int.* **2025**, *200*, 109479. [CrossRef]
81. Si, T.; Chen, X.; Yuan, R.; Pan, S.; Wang, Y.; Bian, R.; Liu, X.; Zhang, X.; Joseph, S.; Li, L.; et al. Iron-modified biochars and their aging reduce soil cadmium mobility and inhibit rice cadmium uptake by promoting soil iron redox cycling. *J. Environ. Manag.* **2024**, *370*, 122848. [CrossRef]
82. Li, Y.; Ning, J.; Li, Q.; Li, L.; Bolan, N.S.; Singh, B.P.; Wang, H. Effects of iron and nitrogen-coupled cycles on cadmium availability in acidic paddy soil from Southern China. *J. Soils Sediments* **2023**, *23*, 431–445. [CrossRef]
83. Uchimiya, M.; Lima, I.M.; Klasson, K.T.; Chang, S.; Wartelle, L.H.; Rodgers, J.E. Contaminant Immobilization and Nutrient Release by Biochar Soil Amendment: Roles of Natural Organic Matter. *Chemosphere* **2010**, *80*, 935–940. [CrossRef] [PubMed]